Ultramicroscopy 130 (2013) 13–28

Contents lists available at SciVerse ScienceDirect

Ultramicroscopy

journal homepage: www.elsevier.com/locate/ultramic

A monochromatic, aberration-corrected, dual-beam low energy electron microscope

Marian Mankos*, Khashayar Shadman

Electron Optica Inc., 1000 Elwell Court #110, Palo Alto, CA 94303, United States

ARTICLE INFO

Available online 21 March 2013

Keywords:
Low energy electron microscopy
Monochromator
Aberration correction
Dual beam illumination
DNA sequencing
Contrast

ABSTRACT

The monochromatic, aberration-corrected, dual-beam low energy electron microscope (MAD-LEEM) is a novel instrument aimed at imaging of nanostructures and surfaces at sub-nanometer resolution that includes a monochromator, aberration corrector and dual beam illumination. The monochromator reduces the energy spread of the illuminating electron beam, which significantly improves spectroscopic and spatial resolution. The aberration corrector utilizes an electron mirror with negative aberrations that can be used to compensate the aberrations of the LEEM objective lens for a range of electron energies. Dual flood illumination eliminates charging generated when a conventional LEEM is used to image insulating specimens. MAD-LEEM is designed for the purpose of imaging biological and insulating specimens, which are difficult to image with conventional LEEM, Low-Voltage SEM, and TEM instruments. The MAD-LEEM instrument can also be used as a general purpose LEEM with significantly improved resolution. The low impact energy of the electrons is critical for avoiding beam damage, as high energy electrons with keV kinetic energies used in SEMs and TEMs cause irreversible change to many specimens, in particular biological materials. A potential application for MAD-LEEM is in DNA sequencing, which demands imaging techniques that enable DNA sequencing at high resolution and speed, and at low cost. The key advantages of the MAD-LEEM approach for this application are the low electron impact energies, the long read lengths, and the absence of heavy-atom DNA labeling. Image contrast simulations of the detectability of individual nucleotides in a DNA strand have been developed in order to refine the optics blur and DNA base contrast requirements for this application.

1. Introduction

Low energy electron microscopy is a technique for imaging electrons that are reflected by the specimen. The technique was developed in the 1980s by professor E. Bauer's group [1]. In Fig. 1, a schematic diagram of a LEEM is shown. The illuminating electrons are emitted from the surface of a cathode, accelerated to their final beam energy, typically 10–25 keV, and focused into a beam separator. The beam separator, a magnetic prism array, bends the electron beam towards the axis of the objective lens. The immersion objective lens decelerates the electrons to a landing energy ranging from 0 eV to a few 100 eV and illuminates the substrate surface with a broad beam. In the opposite direction, moving away from the substrate, the objective lens simultaneously accelerates the reflected and emitted electrons and magnifies the image. As the electrons reenter the beam separator, they are deflected into the projection optics, which further magnifies the image on a scintillating screen. The image formed on the screen is then viewed by a CCD camera and saved on a computer. The extremely low energy of the illuminating electrons makes LEEM an exquisitely sensitive surface imaging technique, capable of imaging single atomic layers with high contrast [2]. Furthermore, the low electron impact energies prevent radiation damage to sensitive samples such as biological molecules. The main drawbacks of LEEM are its susceptibility to chromatic aberrations and charging effects. In spite of the short deBroglie wavelength, which is in the range of Angstroms, the lateral resolution of conventional LEEM instruments is limited to a few nm. In addition, when a conventional LEEM is used to image insulating specimens, sample charging adversely impacts the low energy electron beam, and blurs and distorts the image.

MAD-LEEM is a novel instrument that aims to overcome the aforementioned drawbacks associated with present-day LEEM. The instrument utilizes an energy filtering mechanism to reduce the energy spread of the electron beam to 25 meV or less. It also employs electron mirrors as aberration correcting elements to achieve sub-nm resolution over a relatively large field of view. Last, it illuminates the sample with a second overlapping electron beam with a different landing energy to neutralize the charge deposited by the imaging beam, thereby eliminating surface charging.

* Corresponding author.
E-mail address: marian@electronoptica.com (M. Mankos).

0304-3991/$ - see front matter © 2013 Elsevier B.V. All rights reserved.
http://dx.doi.org/10.1016/j.ultramic.2013.02.018

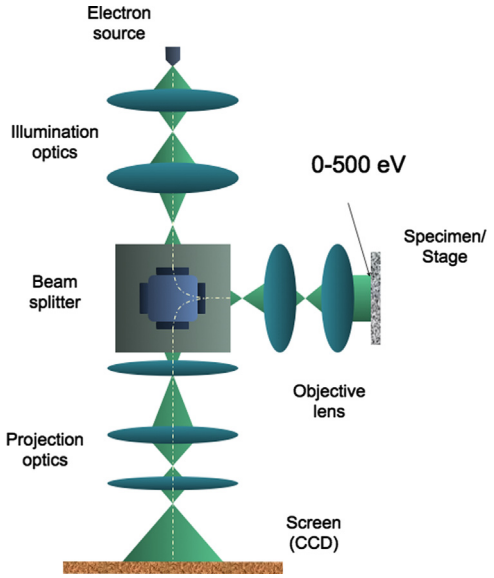

Fig. 1. Schematic layout of a LEEM column.

2. Electron-optical column

A schematic layout of the MAD-LEEM electron-optical column, shown in Fig. 2 represents the conceptual design of the MAD-LEEM column and shows the critical electron-optical elements needed to illustrate the imaging principles. Many of the elements typically present in a detailed column design, e.g transfer and field lenses, alignment and stigmation coils, etc. are omitted here for clarity. The column contains two independent illumination beams, a monochromator, and an aberration corrector which are combined into a single column by beam separators. The beam separators are based on compact, double-focusing magnetic prism arrays composed of uniform magnetic fields of different strength and length. Each separator quadrant deflects the beam by 90 degrees and transfers stigmatically two planes, the diffraction (slit) and (achromatic) image plane, with unit magnification. The excitations of the coils are chosen so that the prism behaves as a thick, round field lens along the curved axis and bends the beam by 90 degrees. The aberration contribution of the individual beam separators is typically minimized by placing a highly-magnified image at the achromatic plane at the center of this field lens. The two illumination beams are for imaging the sample and for mitigating sample charging. The imaging beam optics includes a monochromator that reduces the electron energy spread to 25 meV or less. The main beam separator deflects both beams towards the objective lens, where the electrons are decelerated and focused to form parallel flood beams. The electrons are back-scattered by the specimen, reaccelerated, and focused by the objective lens to form an aberrated image. The lower beam separator transports the image formed by the back-scattered electrons first into a symmetry mirror that compensates for the separator energy dispersion and then into a mirror aberration corrector (MAC) that corrects the spherical and chromatic aberrations of the objective lens. The specimen image is transferred from the center of the beam separator into the object/image plane of the MAC. The MAC images the specimen image onto itself, without forming an intermediate image in the MAC. A field lens placed at the object/image plane of the MAC is used to focus the diffraction/slit plane and control the field rays. The MAC is then set to cancel the combined aberrations of the objective lens and any intermediate transfer and field lenses. Electrons reflected by the aberration corrector are then transported back through the beam separators into the projection optics, which magnifies the image on a viewing screen. In general, a highly magnified image of the sample surface is placed at the center achromatic plane of the beam separators, while the diffraction pattern is placed at the energy-dispersed separator slit plane. On the illumination side, the source image is transferred via the beam separator slit planes into the objective lens back-focal plane, while its angular distribution is transferred via beam separator achromatic planes and used to illuminate the specimen. The justifications for the new features provided by this instrument are described in more detail below.

2.1. Monochromator

Commonly used electron sources such as thermionic emitters (W, LaB_6) or thermally assisted (Schottky) field emitters produce an electron beam with an energy spread in the range of 0.5 eV–2 eV. In order to obtain detailed information about the chemical composition, interatomic bonding, and local electronic states of macromolecules, an energy resolution of 0.2 eV or less is necessary [3]. Thus, a monochromator is needed to reduce the energy spread of the illuminating beam [4,5]. We have developed a novel monochromator [6] utilizing a beam separator, an electron mirror and a knife edge aperture, as shown in Fig. 3. This novel monochromator design also has the potential to further improve the spatial resolution of a LEEM, as it reduces the higher order chromatic aberrations, thereby easing the task for the aberration corrector. In addition, the monochromator together with an electron gun can be used as a stand-alone unit [7] to provide a source of monochromatic electrons that can be utilized to significantly improve spatial resolution in Low-Voltage SEM (LVSEM) and improve energy resolution and spectroscopy in energy-filtered TEM.

The electron source, biased at a high negative voltage, emits electrons with an energy spread, ΔE. The beam passes through the beam separator, which deflects the beam into the electron mirror. The electrons with nominal beam energy E_0 are deflected by 90 degrees (solid, green lines), while electrons with a slightly lower energy (dashed red lines) or higher energy (dotted, purple lines) are deflected slightly more or less, respectively, as a result of the energy dispersion of the beam separator. The axial bundle of rays with energies in the range ($E_0-\Delta E$, $E_0+\Delta E$) appears to emanate from a point near the center plane of the beam separator, also known as the achromatic point (plane). The virtual source image is focused at the plane of a knife edge-shaped aperture in order to achieve high energy resolution. As the electrons proceed towards the electron mirror, a knife edge-shaped aperture stops a fraction of the electrons, in this case the electrons with slightly higher energies, $E_0+\Delta E$, as shown in Fig. 3. The transfer lens focuses the achromatic point at the reflection plane of the electron mirror, which reflects all the electrons back into the beam separator and images the virtual source back at the knife edge plane. As the remaining electrons proceed back to the beam separator, the lower energy electrons with energies $E_0-\Delta E$ are stopped by the same knife edge-shaped aperture. This arrangement allows the use of a simple knife edge as the energy selecting device, which is a much simpler and more reliable design when compared to the narrow, often sub-micrometer slits needed in typical monochromator designs. The remaining electrons have a reduced energy spread, which can be adjusted by the knife edge position. These electrons reenter the beam separator and are deflected a second time by 90 degrees onto the axis of the electron source. After the double pass through the beam separator and the electron mirror, the dispersion introduced by the monochromator vanishes due to symmetry, which is desirable for high resolution imaging. Without the second pass through the beam separator, the beam would acquire energy dispersion, which is detrimental for high resolution imaging in the remaining optics as cross-term aberrations between the

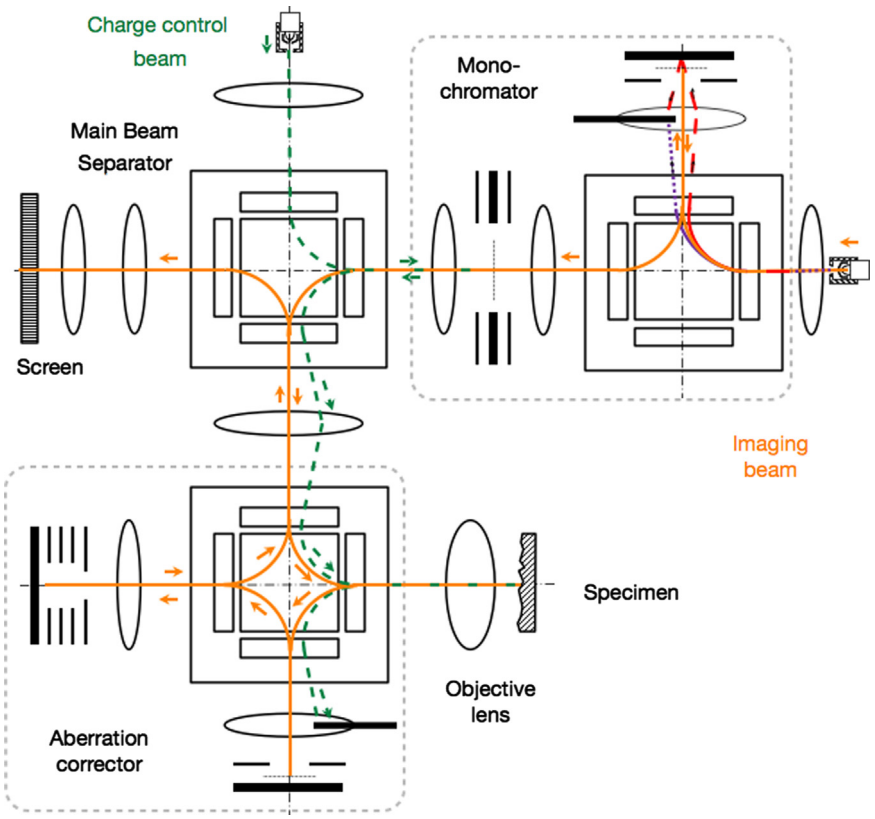

Fig. 2. Electron-optical diagram of the MAD-LEEM column.

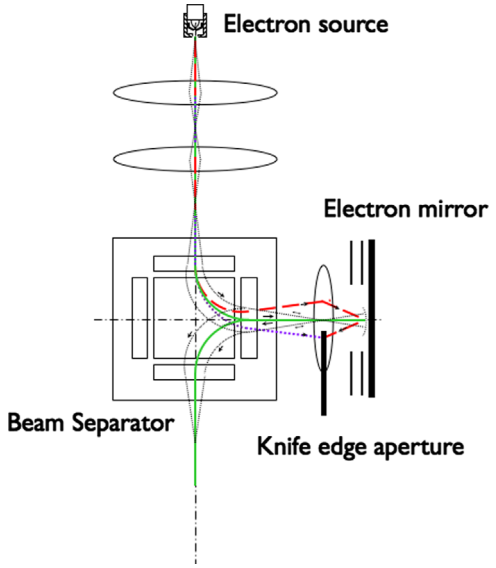

Fig. 3. Electron-optical diagram of a monochromator utilizing a magnetic prism beam separator, electron mirror and knife edge.

dispersion and lens aberrations cannot be corrected by the aberration corrector.

2.2. *Aberration corrector*

The spatial resolution that is achieved in practice in a LEEM without aberration correction is between 4 and 5 nm. At very low electron energies, the resolution is limited by diffraction because of the inverse square root relationship between wavelength and energy: at 1 eV, for example, the electron deBroglie wavelength is 1.2 nm. At an electron energy of 150 eV, the wavelength falls to 0.1 nm, and chromatic and spherical aberrations limit the achievable resolution. Although the monochromator reduces the chromatic aberration significantly, the reduction in the energy spread is not sufficient to improve the resolution to values below 1 nm. As a result, an aberration corrector is required [3,8].

Scherzer in 1936 established that chromatic and spherical aberrations of static round lenses are unavoidable in the absence of space charge and flight reversal [9]. Since then, multiple paths to aberration correction have been pursued, including multipole lenses [10,11], time-dependent fields, charged foils and grids, as well as electron mirrors [12]. A LEEM already includes a path reversal in the objective lens, so the MAC is a natural choice.

In an aberration-corrected LEEM, the spatial resolution can be improved by eliminating one or more aberrations of the objective lens. Conventional rotationally symmetric electron lenses focus more strongly electron rays with larger entrance slopes and lower energies, resulting in positive spherical and chromatic aberration coefficients. Electron mirrors, on the other hand, can be adjusted to focus more weakly the aforementioned rays, thus yielding negative spherical and chromatic aberration coefficients. Schmidt and Tromp utilized a tetrode MAC [13] that eliminates both the chromatic and spherical aberration of the objective lens and experimentally improved the resolution to about 2 nm [14,15]. With the primary spherical and chromatic aberrations eliminated by the MAC, the resolution is determined by diffraction and the remaining higher rank chromatic and 5th order geometric aberrations.

The electron-optical properties of the objective lens ultimately limit the resolution attainable in a LEEM. The specimen is biased at a high negative voltage (tens of kV) and is thereby immersed in a high electrostatic field. This field when combined with the effect of the objective lens produces a magnified image of the specimen surface. Initially, both electrostatic and magnetic objective lenses

were considered. However, the substantially larger aberration coefficients of the pure electrostatic lens removed it from further consideration. The geometry of the magnetic objective lens selected for this microscope is shown in Fig. 4.

The objective lens has an accelerating field of approximately 5 kV/mm at the specimen surface and produces a beam energy of 20 keV. Higher electric fields would improve the resolution; however, they would also present a risk for arcing. The geometry of the electrodes and polepieces was chosen to give a practical lens design capable of forming a magnified image with an object-to-image distance of about 250 mm. The electrode and polepiece geometry utilizes designs optimized for LEEM/PEEM. The equipotential distribution of the electrostatic field and of the flux density is also shown in Fig. 4. The magnetic lens is designed to produce a negligible magnetic field at the substrate in order to minimize aberrations in the diffraction plane. The lower electric field and the vanishing magnetic field at the sample increases the focal length of the objective lens and thereby the spherical aberration. The larger spherical aberration of this lens, however, can still be eliminated by the aberration corrector. Objective lenses designed with higher field strengths have optical advantages and can be considered in later design stages.

The specialized software package MIRROR DA [16] developed by MEBS, Ltd. has been used for the aberration analysis of the objective lenses and of the electron mirrors that are used for aberration correction. The differential algebra-based (DA) software package computes aberrations of electron mirrors of any order and with any symmetry, and can handle combinations of electron mirrors and electron lenses in a unified way. Results computed with MIRROR DA were shown to be in good agreement with those extracted by direct ray tracing with relative deviations of less than 0.065% for all primary aberration coefficients [16]. Table 1 shows the computed values of the key objective lens aberration coefficients (referred to the image plane) obtained by MIRROR DA for an electron energy of 1, 10 and 100 eV, and with the image plane at a distance of 260 mm from the substrate surface.

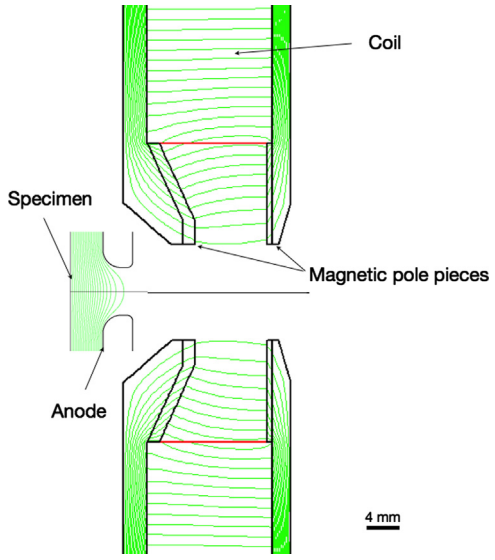

Fig. 4. Geometry, and equipotential and flux density distributions of a magnetic LEEM objective lens.

Simulations of electron-optical properties of the magnetic objective lens have been completed for aberrations up to 5th order in order to understand the resolution limit with aberration correction. The result of this analysis for an electron energy of 1, 10 and 100 eV, with an initial energy spread of 0.25 eV and a field of view of 2 μm on the specimen is shown in Fig. 5. This figure shows plots of all aberrations up to 5th order that are larger than 0.1 nm as a function of the emission angle. The 3rd order geometric and (2nd rank) chromatic aberrations are drawn in dashed lines, while 5th order aberrations are drawn in dotted lines. The total blur is then obtained by adding all aberration terms using Gaussian quadrature. Without aberration correction, the blur is limited by the spherical, chromatic and diffraction aberrations to approximately 8 nm at 1 eV, 6 nm at 10 eV and 5 nm at 100 eV electron energy.

In the next step, the tetrode MAC refined by Wan et al. [17] and Tromp et al. [15] was analyzed. This MAC, shown in Fig. 6, consists of four electrodes: a mirror electrode maintained at a potential more negative than the electron source, two intermediate aperture electrodes, and a ground electrode. In our case, the latter three electrodes have a bore diameter of 8 mm. The potential of the mirror as well as of the two intermediate electrodes can be varied to independently set the focus and simultaneously adjust the primary spherical (C_s) and chromatic (C_c) aberration coefficients of the tetrode MAC. In this example, the focus of the MAC is set to produce a 1x magnified image at the object plane at a distance of 240 mm from the mirror electrode. Once the focus is set, the tetrode MAC spherical and chromatic aberration coefficients are fine-tuned iteratively to cancel aberrations of the combined magnetic objective lens. As the aberration coefficients of the objective lens are strongly dependent on the electron energy, the tuning procedure is carried out for each energy of interest and the appropriate set of MAC electrode potentials is found. With the aberration corrector switched on and the electrode potentials set to the values shown in Fig. 6, the blur is now limited by diffraction, 3rd and 4th rank chromatic and 5th order spherical aberrations to approximately 4.5 nm at 1 eV, 2.5 nm at 10 eV, and 1.5 nm at 100 eV electron energy, as shown in Fig. 7.

In the MAD-LEEM optics, the built-in monochromator lowers the energy spread of the illuminating electrons to 25 meV, which further reduces the higher rank chromatic aberrations, in particular at low landing energies. This reduces the blur further, and diffraction and 5th order spherical aberration become the dominant aberrations. The impact of the monochromator is less noticeable at higher electron energies as the relative contribution of chromatic aberrations is reduced.

The reduction of the higher rank chromatic aberrations is rather important, in particular in the case of an objective lens

Table 1
Electron-optical properties of objective lenses with aberration correction at 1 eV electron energy.

Parameter	1 eV	10 eV	100 eV
Electron energy			
Magnification	9.49	9.57	9.85
3rd order spherical aberration coeff. [m]	14,279	11,279	10,405
2nd rank chromatic aberration coeff. [m]	−52.59	−18.67	−7.99
5th order spherical aberration coeff. [m]	-3.638×10^{10}	-2.973×10^{9}	-2.644×10^{8}
3rd rank chromatic aberration coeff. [m]	−275,505	10,563	511
4th rank chromatic aberration coeff. [m]	4.294×10^{8}	3.365×10^{7}	2.998×10^{6}

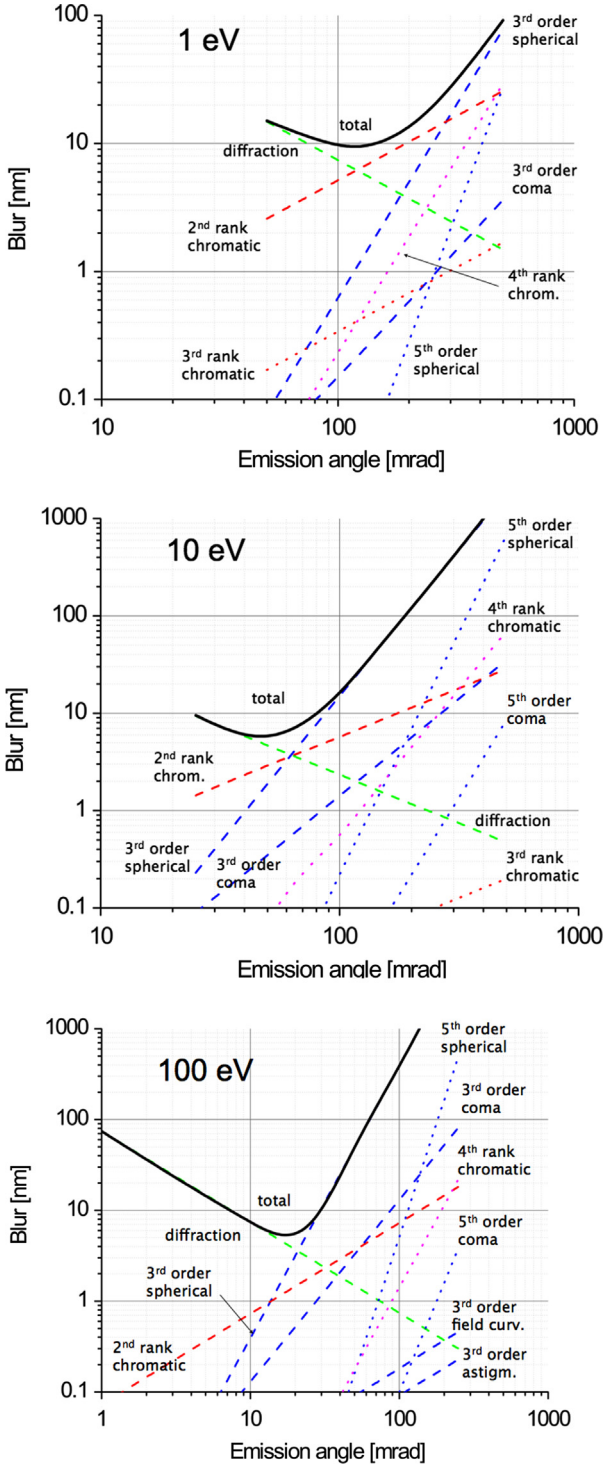

Fig. 5. Aberrations of magnetic objective lens as function of electron emission angle for emission energies of 1, 10 and 100 eV, $\Delta E = 0.25$ eV, and field of view of 2 μm.

with larger spherical aberrations. With the higher chromatic aberrations minimized by the monochromator, it is in principle possible to further improve the resolution by correcting the now dominant 5th order spherical aberration by replacing the tetrode MAC with an improved aberration corrector, a pentode MAC. A pentode MAC includes one additional electrode, which provides the needed degree of freedom to correct one additional aberration: in this case, the 5th order spherical aberration. With the pentode MAC, diffraction and the residual 4th rank chromatic aberration of 3rd order (proportional to the cube of the angle and linear in energy spread) and 5th order coma are then the remaining aberrations, as shown in Fig. 8. Work is currently in progress to optimize the pentode MAC. It is anticipated that the optimization will reduce the blur to approximately 2.5 nm at 1 eV, 1.2 nm at 10 eV, and 0.7 nm at 100 eV landing energy. Further significant improvement in resolution is then achievable only by reducing the diffraction aberration, which can be accomplished by increasing the landing energy of the electrons to a few 100 eV.

In the calculations above we have ignored the contributions from the transfer optics between the cathode objective lens and the MAC. For a detailed column design, all the intermediate optical elements must be taken into account and the MAC must be tuned to correct the net aberrations of all the elements from objective lens to MAC.

2.3. Dual beam illumination

The MAD-LEEM features a dual beam approach that eliminates the risk of charging the specimen by illuminating it with two superimposed flood beams with opposing effects. In a dual-beam LEEM, originally proposed in the early 1990s by L.H. Veneklasen, two electron beams with different landing energies are used to mitigate the charging effect. When an insulating specimen is illuminated with a low energy mirror electron beam with landing energy near 0 eV, a fraction of the electrons is mirrored and the remainder is absorbed, charging the surface negatively. When a higher energy electron beam (few 100 eV) is used, secondary electrons are emitted, and the electron yield can exceed 1, charging the surface positively. However, when these two electron beams are superimposed on the substrate, charging effects can be neutralized. Multiple electron-optical implementations of a LEEM with dual-beam illumination have been proposed and developed [18–20]. Several dual-beam LEEM prototypes have been successfully designed and built, and the dual-beam charge control approach has been demonstrated experimentally on a variety of samples, including oxide structures on Si, resist-coated wafers, and quartz imprint masks [18]. The challenge is to devise an electron-optical design that fits into the system layout and can deliver overlapping illumination of both electron electron beams at preferably normal incidence on the specimen; in other words, a system that combines two parallel electron beams with different energies and beam currents at the specimen surface.

The illumination configuration shown in Fig. 2 includes two perpendicular branches which are joined by the main magnetic beam separator. The first, vertical branch includes an electron gun that generates the charge balance mirror beam with a lower potential energy. The charge balance mirror beam is deflected by the main beam separator by 90 degrees into the horizontal axis and enters an electrostatic Einzel lens configured as an electron mirror, where the center electrode is biased slightly more negative than the first electron gun to reflect the mirror beam back towards the main beam separator. In order to accommodate the 90 degree deflection of the mirror beam towards the Einzel lens, the strength of one of the elements of the beam separator is reduced.

The second electron gun, biased more negatively than the first electron gun by typically 100–300 V, generates the imaging beam, which passes through the mirror Einzel lens and into the main beam separator. The imaging beam is deflected by the main beam separator by 90 degrees, while the mirror beam is deflected by slightly more than 90 degrees, typically a fraction of a degree to a few degrees, due to the energy dispersion of the main beam separator. In order to compensate for this and assure that the two beams are coaxial when they pass through the objective lens and illuminate the specimen, the mirror beam is focused by a field lens that couples the main beam separator to the lower beam separator.

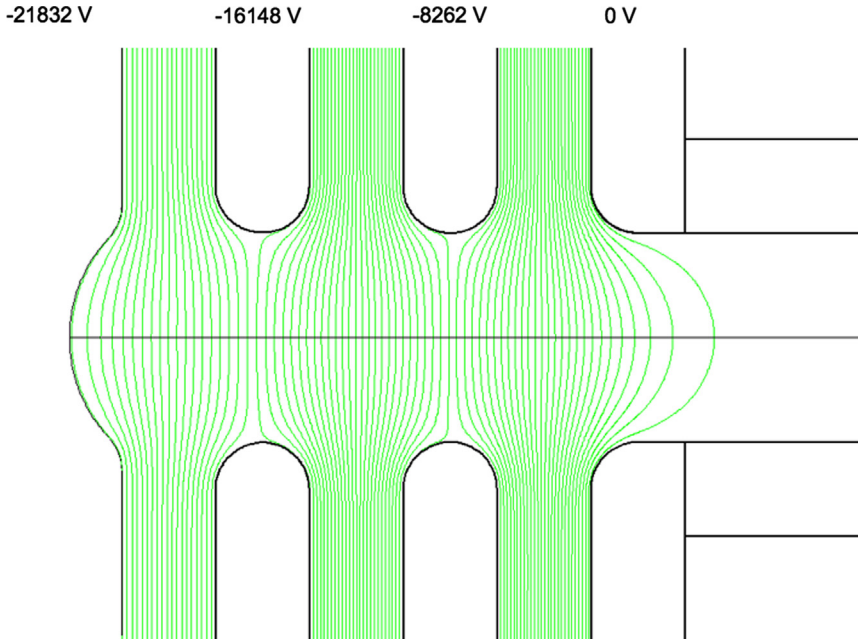

Fig. 6. Geometry and equipotential distribution of a tetrode MAC.

3. DNA sequencing application

The determination of the entire sequence of bases in DNA is one of the fundamental problems of biology and genome research. Currently established sequencing technologies based on capillary array electrophoresis and cyclic array sequencing offer such analytical capability, and 2nd generation sequencers are approaching a cost of $10,000/genome. Despite the tremendous progress in sequencing technology, genome sequencing is still costly and time consuming. One key drawback is that these technologies identify only 10–1000 bases out of the 3 billion base pairs in the human genome in a given sequence segment or read. Another key drawback is the relatively large raw read error rate.

Transmission Electron Microscopy (TEM) is a technique that has been proposed for increasing the read length and accuracy of DNA sequences [21,22]. The TEM approach images the electrons that are transmitted through the specimen. It relies on high electron energies (80–300 keV) to achieve sub-nanometer resolution. The high impact energy, however, not only produces radiation damage, it necessitates the use of heavy atom labels to provide contrast in the image of the nucleotides. The radiation damage limits the electron dose and thereby the throughput. Furthermore, the complications associated with reliably labeling the bases leads to significant read errors. An approach capable of imaging DNA without radiation damage and without labeling is thus highly desirable. The MAD-LEEM approach has several key advantages when compared to these TEM techniques: low electron landing energy, potential for label-free nucleotide specific contrast, and precise charge balance.

The low landing energy of electrons in a LEEM is critical for avoiding radiation damage and achieving high exposure doses, as high energy (>1 keV) electrons cause irreversible damage to biological molecules. Experimental work carried out by Fink's group suggests that DNA withstands electron radiation with electron energies in the range from 60 to 230 eV, despite a vast dose of 10^8 electrons/nm^2 accumulated over more than one hour [23]. A high electron dose is critical for achieving high throughput, as throughput scales directly with electron dose.

In the MAD-LEEM design, a monochromator is introduced into the illumination optics, which is key to probing and differentiating the electronic states of individual nucleotides. Theoretical studies using density functional theory computations of the internal electronic structure of single DNA bases adsorbed on a Cu(111) surface, for example, show a diversity of electronic structures for each of the individual nucleotides [24] that can potentially result in different electron reflectivity spectra analogous to Hibino's approach for determining the graphite thickness [2]. The characteristic signature imprinted in the reflectivity spectra has the potential of providing contrast in the images of unlabeled bases, which can be utilized to sequence the nucleotides in a DNA strand. The MAD-LEEM approach with monochromatic, low energy illumination is ideally suited to deliver the resolution and to achieve the necessary contrast given that the energy levels are expected to vary on the order of a fraction of 1 eV. Early experimental results on LEEM imaging of DNA structures without labels immobilized on gold substrates [29] demonstrate that high contrast is indeed achievable at low electron energies in the range of 1–10 eV.

The conductivity of DNA is claimed to vary from that of an insulator to that of a superconductor [25,26], depending on the substrate and the way DNA is attached to the electrodes. When a partially or fully insulating macromolecule is imaged with an electron beam, the imbalance between the arriving and leaving electron flux may cause the DNA strand to charge, resulting in added blur. The MAD-LEEM design incorporates a charge balance mirror beam that prevents the charging of individual molecules. In case the individual DNA strands are sufficiently conductive to prevent charging, the mirror beam can be turned off.

DNA consists of two long polymer strands, entwined like vines in the shape of a double helix [27]. The backbone of the strand is made of sugars and phosphate groups, and attached to each sugar is one of four types of molecules called bases: adenine (A), cytosine (C), guanine (G) and thymine (T). The sequence of these four bases along the backbone encodes the genetic information. In a DNA double helix, the bases form complementary base pairs: A forms a base pair with T, and G forms a base pair with C. The base pairs are bonded by relatively weak hydrogen bonds, and thus the two strands of DNA in a double helix can be pulled apart like a zipper by enzymes, mechanical forces, or high temperature. As a result of the complementary base pairing, all the information in the double-stranded sequence of a DNA (ds-DNA) helix is

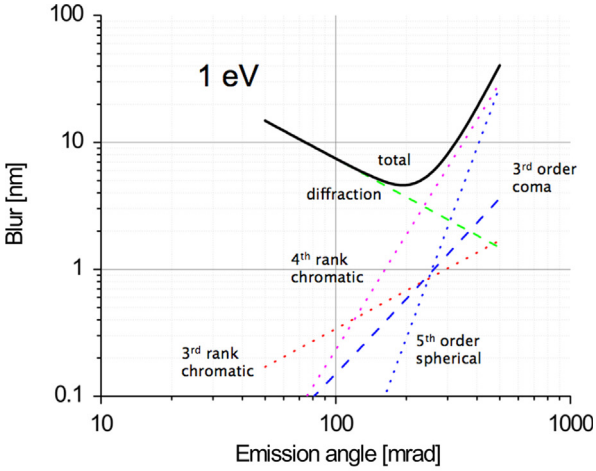

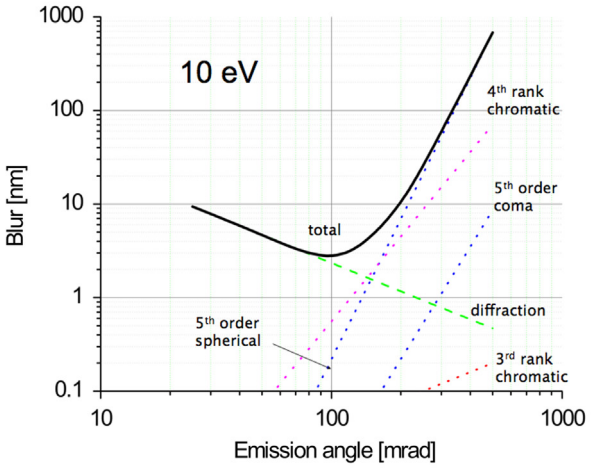

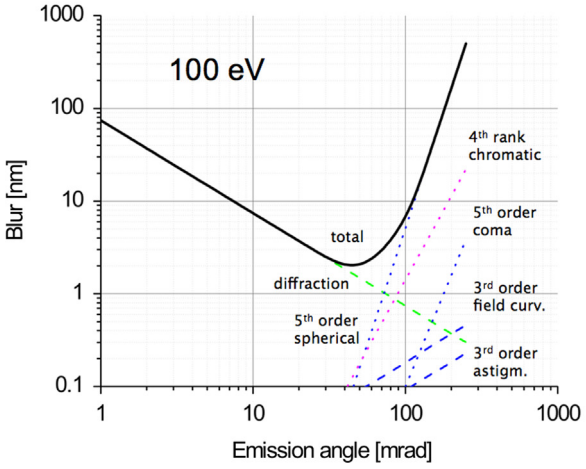

Fig. 7. Magnetic objective lens aberrations with corrected primary spherical and chromatic aberrations as function of electron emission angle for emission energies of 1, 10 and 100 eV, $\Delta E = 0.25$ eV, and field of view of 2 μm.

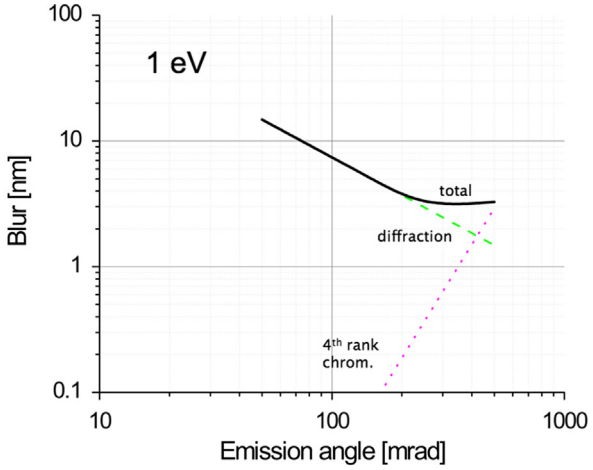

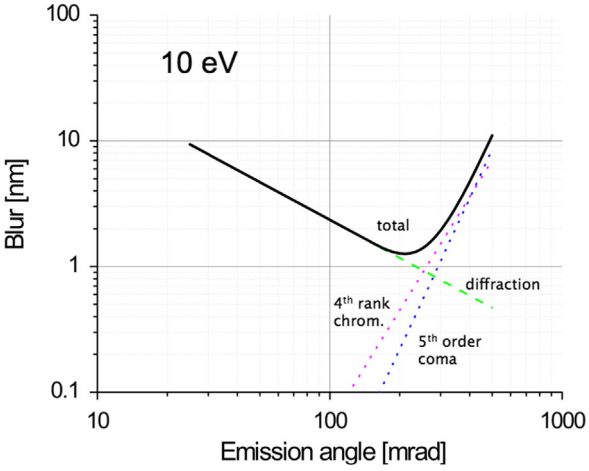

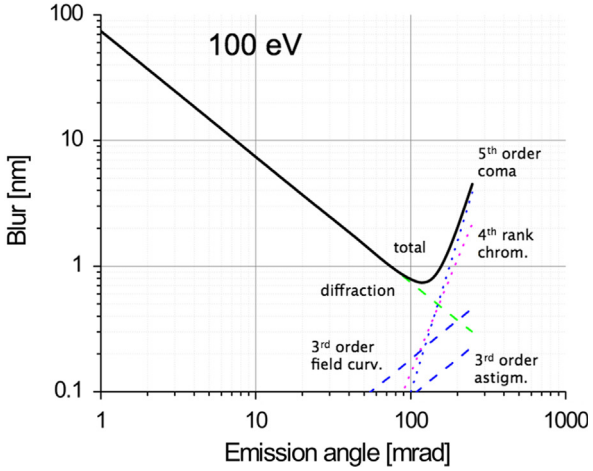

Fig. 8. Magnetic objective lens aberrations with corrected 3rd and 5th order spherical and primary chromatic aberrations and 25 meV monochromaticity as function of electron emission angle for emission energies of 1, 10 and 100 eV, and field of view of 2 μm.

duplicated on each single strand. This means that one can in principle image either the double helix or a single strand (ss-DNA) for DNA sequencing.

The outline for sequencing DNA with an electron microscope is shown in Fig. 9. First, a substrate with densely packed, stretched out strands of DNA is prepared, using, for example, molecular combing techniques [28]. Molecular combing attaches an array of single DNA molecules with a random-coil configuration to a silanised substrate by their extremities. When the substrate is slowly removed from the solution, arrays of thousands of combed molecules as long as 5 million base pairs are uniformly stretched and aligned by the receding air–water meniscus and adhere to the substrate along their length, thus preventing retraction. In

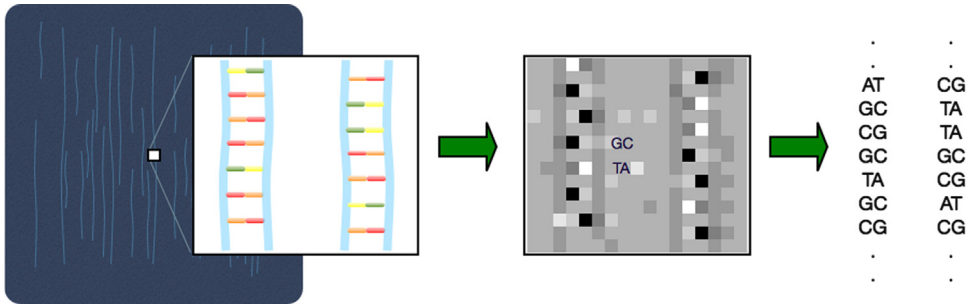

Fig. 9. Sequencing strategy using a MAD-LEEM, from left to right: substrate with stretched out ds-DNA, magnified view of sections of two ds-DNA molecules, anticipated nucleotide-specific contrast, identified DNA base sequence.

addition, the base-to-base spacing increases from 0.34 to 0.5 nm for ds-DNA and 0.7 nm for ss-DNA. In the next step, the substrate with the attached DNA molecules is inserted into the electron microscope and imaging conditions yielding nucleotide-specific contrast are obtained by tuning the imaging parameters. For ds-DNA the task is reduced to distinguishing two base pairs (AT and GC) and determining their orientation (AT or TA and GC or CG), due to the complementary nature of base pairs. This reduces the image resolution requirements, since we seek only to distinguish two molecule pairs from each other and do not require the imaging of individual nucleotides. For imaging of ss-DNA, each of the four bases needs to be distinguishable at a pitch of 0.7 nm. In the final step, the acquired gray-level image is analyzed on-the-fly by an image computer. Images of individual bases or pairs are located and correlated with the anticipated contrast, and the base sequence is determined for each DNA strand in the field of view and stored in the computer memory.

4. Contrast simulations

As the existing reflectivity data is limited to bulk nucleotide oligomers, there is a need to extrapolate the data to what would be found when imaging individual nucleotides in a sequence with the anticipated resolution of MAD-LEEM. The calculation of the electron reflectivity of the nucleotides would require modeling the cross-section presented by the bases to impinging electrons with energies of order or less than 100 eV. Here, a simple approach is taken whereby the bases of the DNA are modeled as features that present an effective, unknown area of interaction that is rectangular in cross-section. Within this area, the bases are assumed to reflect a fraction of the incident electrons as given by a reflectivity coefficient derived from imaging bulk samples. The analysis is simplified further by assuming that the imaging of the reflected electrons is incoherent. As such, the bases are viewed as 2D intensity objects. Furthermore, any anomalous contribution to the contrast from interference by the electrons reflected from the background surface is neglected. The reflectivity contrast of the individual bases is then calculated as a function of the optical blur and pixel size in relation to the size of the base and the pitch in the sequence. Combined with a model for the system noise, the analysis produces an estimate for the read-error in sequencing for a given imaging condition, sequence geometry, and nominal reflectivity contrast obtained from bulk nucleotide oligomers.

4.1. Imaging electrons mirrored by features on a flat surface

For an electron beam of uniform current density $\bar{J}$ impinging a surface with reflectivity profile $\eta(x)$, the density of electron current that is reflected and imaged onto a detector can be expressed as

$$J(\boldsymbol{x}) = \bar{J}\int d\boldsymbol{x}' f(\boldsymbol{x}-\boldsymbol{x}')\cdot\eta(\boldsymbol{x}') \tag{1}$$

where $f(\boldsymbol{x})$ is the point-spread function (PSF) of the imaging arm of the microscope. Here, the image is assumed to be corrected for distortion, and all spatial quantities are to be evaluated at the object surface, where the features lie. The current deposited onto a pixel within a 2D array on the detector is then

$$I_{\boldsymbol{n}} = \int_{\boldsymbol{x}_{\boldsymbol{n}-1/2}}^{\boldsymbol{x}_{\boldsymbol{n}+1/2}} d\boldsymbol{x}\, J(\boldsymbol{x}) = \int \boldsymbol{dx} R(\boldsymbol{x}-\boldsymbol{x}_{\boldsymbol{n}},\boldsymbol{p}) J(\boldsymbol{x}) \tag{2}$$

where $\boldsymbol{x}_{\boldsymbol{n}} = (n_1 p_1, n_2 p_2)$ is the location of the pixel center with pixel dimensions $\boldsymbol{p} = (p_1, p_2)$, and $R(\boldsymbol{x},\boldsymbol{p})$ denotes the 2D *Rect* function

$$R(\boldsymbol{x},\boldsymbol{p}) \equiv \prod_i R(x_i, p_i) \tag{3}$$

where

$$R(x_i,p_i) = \begin{pmatrix} 1 & for\ |x_i| \le p_i/2 \\ 0 & for\ |x_i| > p_i/2 \end{pmatrix} \tag{3a}$$

The features are assumed to be resting on a surface with reflectivity η_0. As a result, the reflectivity function comprises the two contributions

$$\eta(\boldsymbol{x}) = \eta_0 + \sum_*(\eta_* - \eta_0) H_*(\boldsymbol{x}-\boldsymbol{x}_*) \tag{4a}$$

where η_* is the feature reflectivity, $H_*(\boldsymbol{x})$ is its reflectivity profile, $\boldsymbol{x}_*$ is the feature center, and the sum is over all features. The contribution to the pixel current from the surface reflectivity is simply

$$I_0 = \eta_0 \bar{J} p_1 p_2. \tag{5}$$

4.1.1. Fourier representation

If the features form an array, then the reflectivity profile will be periodic in nature. Consequently, the convolution integral of Eq. (2) is Fourier decomposed to produce a sum of Fourier modes that efficiently compute the integral. The Fourier representation of Eq. (2) is

$$I_{\boldsymbol{n}} = \bar{J}\int \boldsymbol{dk}\tilde{\eta}(\boldsymbol{k})\tilde{f}(\boldsymbol{k})\tilde{R}(-\boldsymbol{k},\boldsymbol{p}) \tag{2'}$$

where the accent character, tilde, signifies the Fourier transform. In particular, $\tilde{R}$ is the Fourier transform of the *Rect* function

$$\tilde{R}(\boldsymbol{k},\boldsymbol{p}) = \prod_i p_i \mathrm{sinc}\left(2\pi k_i \frac{p_i}{2}\right) \tag{3'}$$

with

$$\mathrm{sinc}x \equiv \left\{ \begin{matrix} \frac{\sin x}{x} & for\ x \ne 0 \\ 1 & for\ x = 0 \end{matrix} \right\}.$$

4.1.2. A Gaussian point-spread function

The Point-Spread function (PSF) resulting from the effects of aberrations, diffraction, and Coulomb interactions in the imaging arm of the microscope is assumed to be separable in the two coordinates, $f(\boldsymbol{x})=f_1(x_1)f_2(x_2)$. It is further assumed that the PSF in each dimension is Gaussian with a standard deviation equal to σ_i; that is

$$f_i(x_i)=\frac{1}{\sqrt{\pi}}\frac{1}{\sqrt{2}\sigma_i}\exp\left[-\left(\frac{x_i}{\sqrt{2}\sigma_i}\right)^2\right] \tag{6a}$$

The Fourier representation of a Gaussian function is itself Gaussian:

$$\tilde{f}_i(k_i)=\exp[-(\pi k_i\sqrt{2}\sigma_i)^2] \tag{6b}$$

For an isotropic Gaussian profile, where $\sigma_1=\sigma_2=\sigma$, the PSF diameter d is defined by the fraction of the current ι it contains:

$$d(\iota)=\sqrt{-8\ln(1-\iota)}\cdot\sigma$$

The Full-Width-Half-Max (FWHM) corresponds to the value of $d(0.5)$ or $2.35\cdot\sigma$ (also true in 1D). In the subsequent sections and figures, the diameter will refer to the value that contains 99% of the current: that is

$$d\equiv d(0.99)\cong 6.07\cdot\sigma$$

This value is a good approximation to the optical blur obtained in the simulations described in Section 2.

4.2. Intensity profile of an array of identical, rectangular features

For an array of identical features distributed along x_1 with pitch γ, the feature reflectivity function has the form

$$\eta'(\boldsymbol{x})\equiv\eta(\boldsymbol{x})-\eta_0=(\eta_*-\eta_0)\sum_m H_*(\boldsymbol{x}-\boldsymbol{x}_*)$$

with

$$\boldsymbol{x}_*=(m\gamma,0)+\boldsymbol{\varepsilon}=(\varepsilon_1+m\gamma,\varepsilon_2)$$

where $\boldsymbol{\varepsilon}$ describes the offset of the feature center from that of a reference pixel. Here, it is assumed that any skew between the pixel and the feature arrays can be eliminated as shown by the geometry in Fig. 10. The Fourier transform of the reflectivity function separates into a product of the contribution from an individual feature, $\tilde{H}_*$, and that from the periodicity of the array; that is

$$\tilde{\eta}'(\boldsymbol{k})=(\eta_*-\eta_0)e^{-2\pi i\boldsymbol{k}\cdot\boldsymbol{\varepsilon}}\tilde{H}_*(\boldsymbol{k})\sum_m e^{-2\pi i m k_1\gamma}$$

Noting the relation

$$\sum_m e^{-2\pi i m\mu}=\sum_m\delta(\mu-m)$$

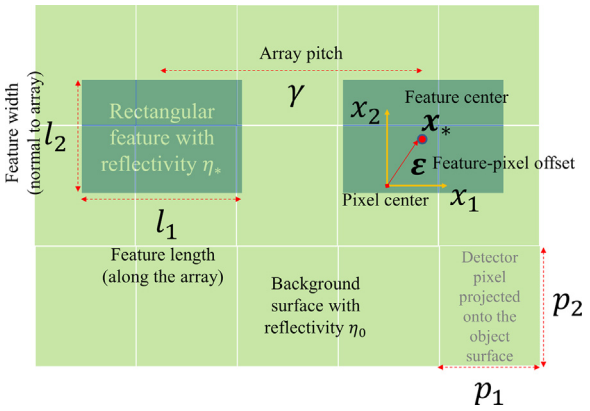

Fig. 10. Feature and pixel geometry, and definitions.

where $\delta(x)$ is the delta-function, the Fourier integral of the sum is evaluated to give

$$I'=c_*I_0\frac{1}{\gamma}\sum_m e^{2\pi i\frac{m}{\gamma}(n_1p_1-\varepsilon_1)}\mathrm{sinc}\left(\pi\frac{m}{\gamma}p_1\right)I_{12}$$

with the nominal, inherent contrast defined as

$$c_*\equiv\frac{\eta_*-\eta_0}{\eta_0}$$

I_0 given by Eq. (5) and

$$I_{12}\equiv\int dk_2 e^{2\pi ik_2(n_2p_2-\varepsilon_2)}\tilde{H}\left(\frac{m}{\gamma},k_2\right)\tilde{f}\left(\frac{m}{\gamma},k_2\right)\mathrm{sinc}(\pi k_2p_2)$$

Introducing the Gaussian PSF and modeling the features to be rectangular with side lengths $\boldsymbol{l}_*=(l_1,l_2)$ separates the normalized pixel current into the product of the profiles parallel and perpendicular to the array direction. Using the following vector to ease the notation

$$\boldsymbol{q}_i\equiv[p_i,\varepsilon_i,l_i]$$

the current is represented as

$$\frac{I'}{I_0}=c_*I_1\left(n_1;\frac{\boldsymbol{q}_1}{\gamma},\frac{\sigma_1}{\gamma}\right)I_2\left(n_2;\frac{\boldsymbol{q}_2}{\sigma_2}\right) \tag{7}$$

with I_1 describing the periodic profile along the array

$$I_1\left(n_1;\frac{\boldsymbol{q}_1}{\gamma},\frac{\sigma_1}{\gamma}\right)\equiv\frac{l_1}{\gamma}\sum_m e^{2\pi im\frac{n_1p_1-\varepsilon_1}{\gamma}}e^{-\left(\pi m\frac{\sqrt{2}\sigma_1}{\gamma}\right)^2}\mathrm{sinc}\left(\pi m\frac{p_1}{\gamma}\right)\mathrm{sinc}\left(\pi m\frac{l_1}{\gamma}\right) \tag{7a}$$

and I_2 describing the profile normal to the array direction

$$I_2\left(n_2;\frac{\boldsymbol{q}_2}{\sigma_2}\right)\equiv\frac{\sqrt{2}\sigma_2}{2p_2}\sum_{s_l,s_p\in\pm1}s_ls_p\left[y\mathrm{erf}y+\frac{1}{\sqrt{\pi}}e^{-y^2}\right]_{y=\frac{n_2p_2-\varepsilon_2+\frac{1}{2}(s_ll_2+s_pp_2)}{\sqrt{2}\sigma_2}} \tag{7b}$$

It should be noted that the expression for I_2 is derived with less difficulty by utilizing the 1D version of Eq. (2).

4.2.1. The limiting case of an isolated rectangular feature

The functional form of I_1 must transform to the form of Eq. (7b) in the limit $\gamma/\sigma_1\to\infty$, where the features are effectively isolated from each other; that is

$$I_1\left(n_1;\frac{\boldsymbol{q}_1}{\gamma},\frac{\sigma_1}{\gamma}\right)\Big|_{\frac{\sigma_1}{\gamma}\to0}=I_2\left(n_1;\frac{\boldsymbol{q}_1}{\sigma_1}\right) \tag{8}$$

The profile of an isolated feature is then described by

$$\frac{I'}{I_0}=c_*I_2\left(n_1;\frac{\boldsymbol{q}_1}{\sigma_1}\right)I_2\left(n_2;\frac{\boldsymbol{q}_2}{\sigma_2}\right). \tag{8a}$$

4.2.2. The practical case of a blurred image

The exponential attenuation of the Fourier modes of I_1 renders the contributions from terms with $|m|\gg\gamma/\sqrt{2}\sigma_1$ inconsequential. In particular, for a practical case where the PSF diameter is sizeable relative to the array pitch

$$\gamma<\sqrt{2}\pi\sigma_1$$

the dominant contribution will come from $|m|\le1$, producing a sinusoidal profile along the array:

$$I_1\cong\frac{l_1}{\gamma}\left\{1+2\left[e^{-\left(\pi\frac{\sqrt{2}\sigma_1}{\gamma}\right)^2}\mathrm{sinc}\left(\pi\frac{p_1}{\gamma}\right)\mathrm{sinc}\left(\pi\frac{l_1}{\gamma}\right)\right]\cos\left(2\pi\frac{n_1p_1-\varepsilon_1}{\gamma}\right)\right\} \tag{9a}$$

The first term contributes to the mean signal, and the ripple in the signal is derived from the second. The maximum attainable variation in the signal is achieved between two pixels that give cosine values of opposite polarity: ±1. For $p_1=\gamma/2$ and $\varepsilon_1=p_1/2$, all pixels see the average intensity l_1/γ and thereby show no

contrast. The impact of the PSF diameter, of the pixel size, and of the feature length on the profile of I_1 is illustrated in Fig. 11A and B for cases in which the pixel size is matched to the pitch; that is for γ/p_1 equal to an integer. Here, the feature centers are located at the intensity maxima. The key point from these figures is the goodness of fit provided by the dominant Fourier mode (open circles) when the PSF diameter remains a healthy fraction of the array pitch.

The profile across the array simplifies as well for a sizeable PSF diameter; that is, for

$$\sqrt{p_2^2+l_2^2} < \sqrt{12}\sigma_2$$

In this regime, Eq. (7b) may be approximated (after some algebra) by a Gaussian profile

$$I_2 \cong \frac{l_2}{\sqrt{2}\sigma_2^*}\frac{1}{\sqrt{\pi}} e^{-\left(\frac{n_2 p_2 - \varepsilon_2}{\sqrt{2}\sigma_2^*}\right)^2} \tag{9b}$$

with an augmented standard deviation due to a convolution of the PSF with the finite extent of the feature and of the pixel in the direction normal to the array:

$$\sigma_2^* \cong \left[1+\frac{1}{24\sigma_2^2}(p_2^2+l_2^2)\right]\sigma_2$$

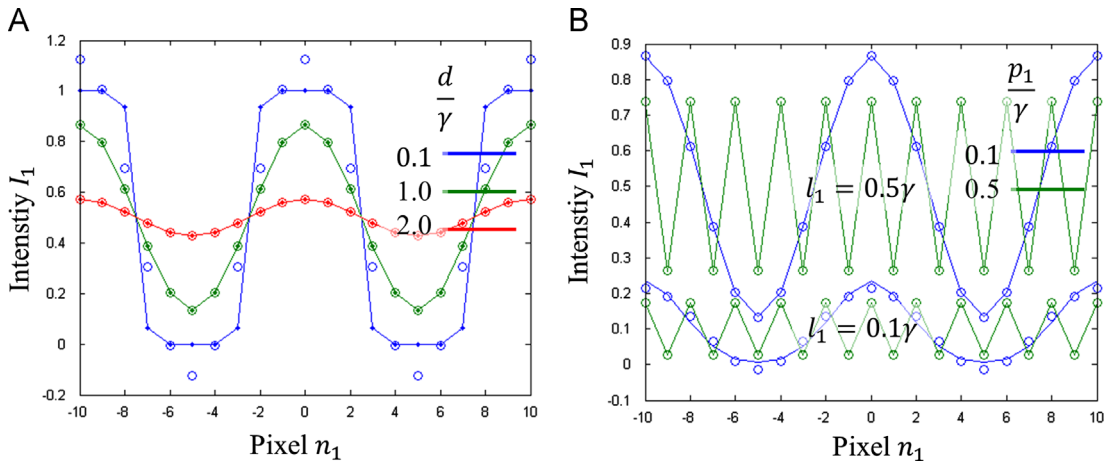

Fig. 11. 1D profile along the array. (●) Exact, all Fourier modes, (○) dominant Fourier mode only. (A) Effect of PSF diameter d_1 for pixel size $p_1 = 0.1\gamma$, feature length $l_1 = 0.5\gamma$, and feature offset $\varepsilon_1 = 0$. (B) Effect of pixel size p_1 and feature length l_1 for PSF diameter $d_1 = \gamma$ and feature offset $\varepsilon_1 = 0$.

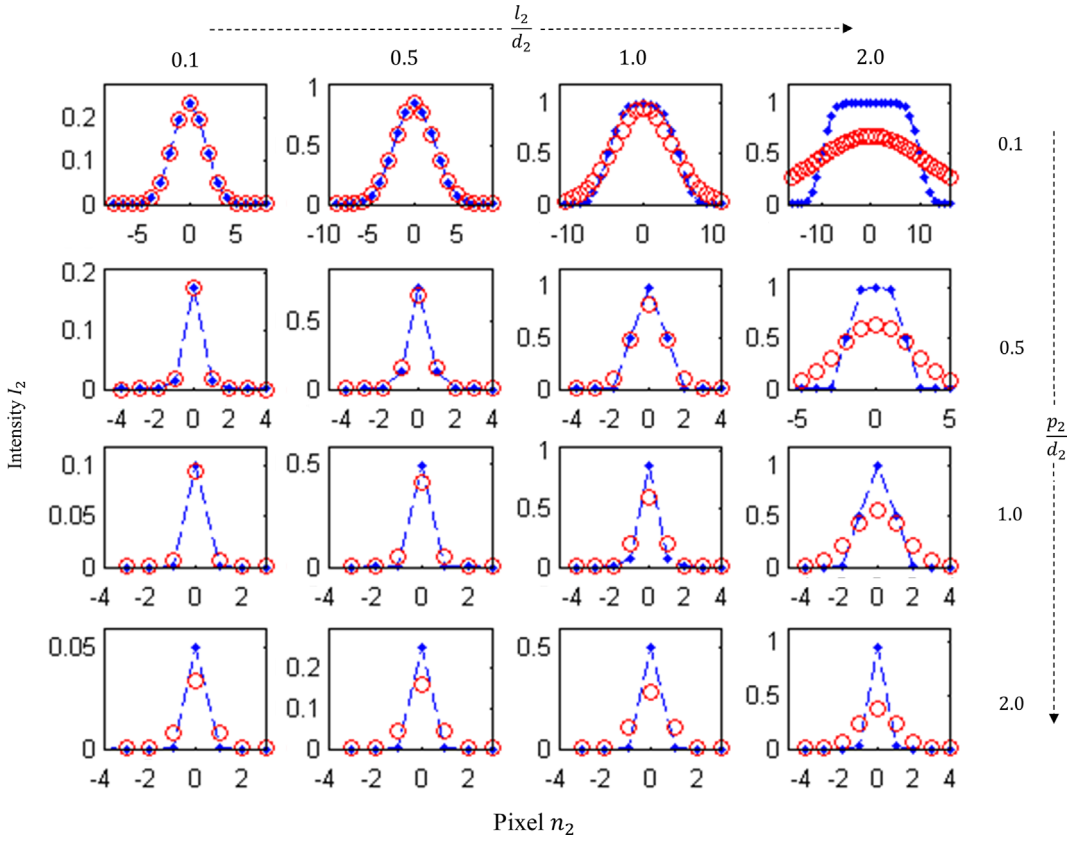

Fig. 12. 1D profiles normal to the array for various feature lengths l_2 and pixel sizes p_2 with offset $\varepsilon_2 = 0$. (●) Exact solution, (○) Gaussian approximation.

The Gaussian fit to the profile of I_2 is depicted for a range of pixel sizes and feature lengths in Fig. 12. Here, the feature center is located at $n_2 = 0$. The profile of I_2 is shown to be well approximated by Eq. (9b) so long as the pixel size and the feature width remain less than or equal to the PSF diameter. The discrepancy between the exact profile and that of the Gaussian approximation is less than 10% of the peak value for p_2, $l_2 \leq 0.5 d_2$ and increases to 30% of the peak value for $p_2 = l_2 = d_2$.

For an isolated feature, the intensity profile along coordinate x_1 adopts the profile of Eq. (9b) as well, making

$$\frac{I'}{I_0} \cong c_* \frac{A_*}{A_\sigma} e^{-\Sigma_i \left(\frac{n_i p_i - \epsilon_i}{\sqrt{2}\sigma_i^*} \right)^2} \tag{10}$$

with $A_* = l_1 l_2$ equal to the feature area and with $A_\sigma = 2\pi\sigma_1^*\sigma_2^*$ equal to the effective area of the PSF, where σ_1^* is the augmented standard deviation along coordinate x_1 (defined analogously to σ_2^*).

4.2.3. The intensity contrast

The intensity contrast is defined by the maximum variation in the normalized intensity profile, $\Delta I/I_0$, and is graphed in Fig. 13, which shows its dependence on the PSF diameter, the pixel size, the feature length, and the feature-pixel offset along the array. The archetype condition chosen for the plots is described by the nominal contrast $c_* = 1$, square pixels ($p_1 = p_2 = p$), and isotropic PSF blur ($d_1 = d_2 = d$). The contrast is shown to decay exponentially with the square of the PSF diameter, highlighting its sensitivity to image resolution. The contrast has a more gradual variation with the pixel size and the feature length, peaking for $p_1 \to 0$ and $l_1 = (\gamma/2)$ and diminishing for $p_1 = m\gamma$ or $l_1 = \gamma$ where the features kiss their neighbors. The glitches with pixel size in the sinc profile are associated with the complex dependence of the extrema in I_1 on the pixel location $p_1 n_1$. For pixel sizes greater than the array pitch ($p_1 > \gamma$), the amplitude oscillates with decreasing magnitude, owing to the $1/p_1$ dependence of the sinc function. The effect of the feature-pixel offset becomes pronounced as the pixel size increases towards the value $\gamma/2$.

4.3. Intensity contrast of two model sequences

Having analyzed the intensity contrast from an array of identical features, two model sequences are readily examined: that of a new feature b embedded in an array of identical features a; and that of an array of alternating features a and b. Here, it is convenient to define the average and difference in the feature reflectivities as

$$\bar{\eta} \equiv \tfrac{1}{2}(\eta_a + \eta_b)$$
$$\tilde{\eta} \equiv \tfrac{1}{2}(\eta_a - \eta_b)$$

with corresponding definitions for the nominal contrast

$$\bar{c} \equiv \tfrac{1}{2}(c_a + c_b) = \tfrac{\bar{\eta} - \eta_0}{\eta_0}$$
$$\tilde{c} \equiv \tfrac{1}{2}(c_a - c_b) = \tfrac{\tilde{\eta}}{\eta_0}$$

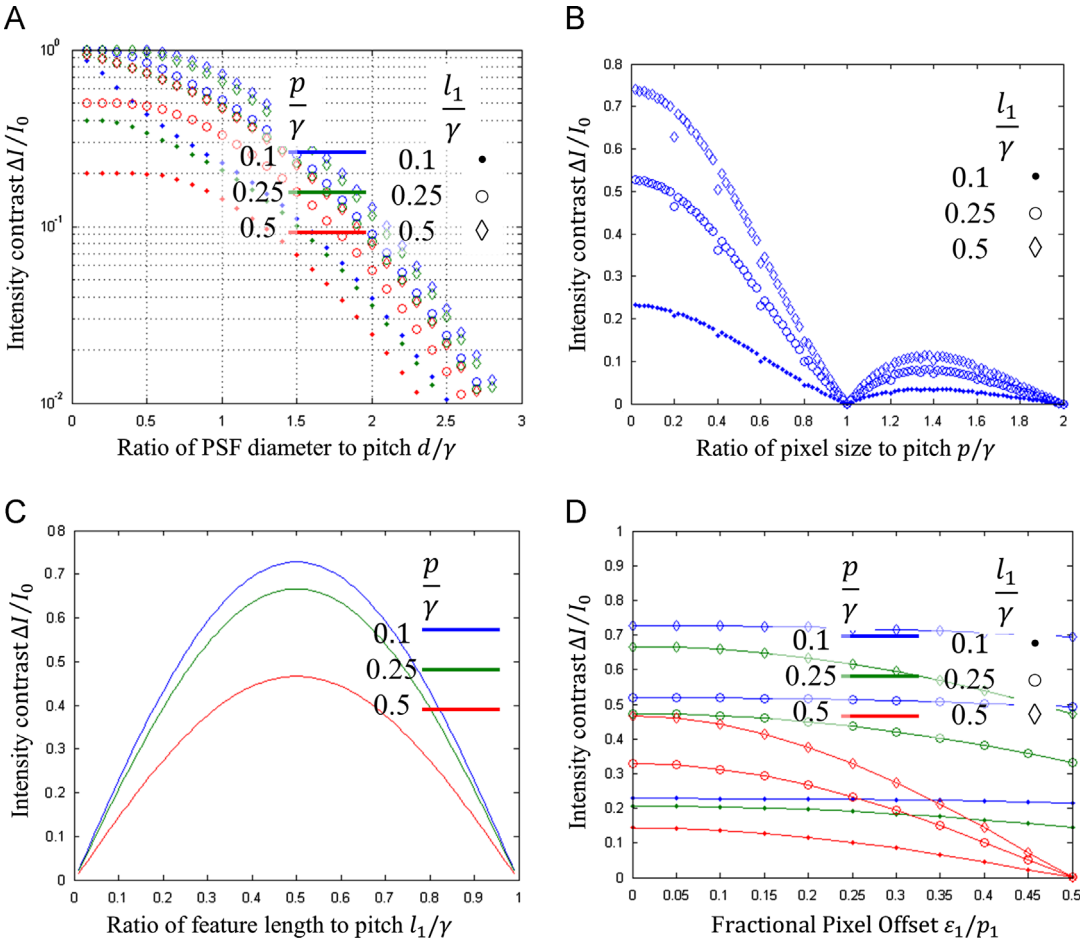

Fig. 13. Effect of the PSF diameter, pixel size, and feature length on the intensity contrast in an array of identical features for nominal contrast $c_* = 1.0$, square pixels $p_1 = p_2 \equiv p$, isotropic PSF $d_1 = d_2 \equiv d$, and feature width $l_2 = \gamma$. (A) Exponential decay in the contrast with the square of the PSF diameter for $\epsilon = 0$. (B) Sinc variation in the contrast with pixel size for $d = \gamma$ and $\epsilon = 0$. (C) Sinusoidal variation in the contrast with feature length for $d = \gamma$ and $\epsilon = 0$. (D) Impact of the feature-pixel offset along the array on the contrast for $d = \gamma$ and $\varepsilon_2 = 0$.

The average intensity of the two features (in bulk) is also defined:

$$\bar{I} \equiv \bar{\eta} \bar{J} p_1 p_2 = \bar{\eta}/\eta_0(I_0) = (1+\bar{c}) I_0$$

Furthermore, a shorthand is adopted to highlight the variables of interest for this exercise:

$$I_1(\varepsilon_1, l_1, \gamma) \equiv I_1\left(n_1; \frac{\boldsymbol{q}_1}{\gamma}, \frac{\sigma_1}{\gamma}\right)$$

$$I_2(\varepsilon_i, l_i) \equiv I_2\left(n_i; \frac{\boldsymbol{q}_i}{\sigma_i}\right), \quad i \in 1, 2.$$

4.3.1. A new feature embedded in an array of identical features

Using the abovementioned variables, the intensity profile of a feature with reflectivity η_b and size $\boldsymbol{l}_b$ that is embedded in an array of features with reflectivity η_a with size $\boldsymbol{l}_a$ is expressed as

$$\frac{I}{I_0} = 1 + c_a\left[I_1(\varepsilon_1, l_{1a}, \gamma) - I_2(\varepsilon_1, l_{1a})\right] I_2(\varepsilon_2, l_{2a}) + c_b I_2(\varepsilon_1, l_{1b}) I_2(\varepsilon_2, l_{2b}) \quad (11)$$

This profile is derived by removing the reflectivity of a single feature a from that of the array and replacing it with the reflectivity of a single feature b. For features of the same size, $\boldsymbol{l}_a = \boldsymbol{l}_b \equiv \boldsymbol{l}$, Eq. (11) reduces to

$$\frac{I}{I_0} = 1 + \{\bar{c} I_1(\varepsilon_1, l_1, \gamma) + \tilde{c}\left[I_1(\varepsilon_1, l_1, \gamma) - 2 I_2(\varepsilon_1, l_1)\right]\} I_2(\varepsilon_2, l_2) \quad (11a)$$

The first term is the profile of an array of identical features having the average reflectivity of features a and b; the second term gives the contrast. There are two natural cases: one where the average reflectivity of the two features equals that of the surface ($\bar{\eta} = \eta_0$), making $\bar{c} = 0$; and one where the background surface goes dark, $\eta_0/\bar{\eta} \to 0$ ($\bar{c} \to \infty$). For the latter case, the above profile (renormalized to $\bar{I}$) becomes

$$\frac{I}{\bar{I}}\Big|_{\eta_0/\bar{\eta} \to 0} \to \left\{I_1(\varepsilon_1, l_1, \gamma) + \frac{\tilde{\eta}}{\bar{\eta}}\left[I_1(\varepsilon_1, l_1, \gamma) - 2 I_2(\varepsilon_1, l_1)\right]\right\} I_2(\varepsilon_2, l_2) \quad (11b)$$

The two profiles are plotted in Fig. 14 for $\tilde{\eta} = 0.5\bar{\eta}$. Notice that the dip in the signal from the new feature is the same for both; however, for a dark surface, the oscillations in the intensity are amplified relative to the dip.

In practice, it is desirable to match the pixel size to the array pitch to eliminate any signal variation that is unrelated to the feature reflectivity. In such cases, I_1 will not contribute to the contrast. The remaining term is proportional to the nominal contrast between the two features, $\tilde{\eta}/\bar{\eta}$. The ratio of the effective to the nominal contrast for the new feature embedded in an array of identical features is then given by

$$\rho \equiv \frac{(I_a - I_b/I_a + I_b)}{(\eta_a - \eta_b/\eta_a + \eta_b)} = \Delta I_2(\varepsilon_1, l_1) \cdot I_2(\varepsilon_2, l_2) \quad (11c)$$

The contrast ratio is always less than one, indicating the degree of loss in the contrast of an embedded feature in an array when imaging with finite optical blur, pixel size, and pixel misalignment. The ratio is graphed against the PSF diameter for a few pixel and feature sizes in Fig. 15. Here, the effect of the feature-pixel offset, $\boldsymbol{\varepsilon}$, is summarized by two curves for the same parameter set, which indicate the values that are one standard deviation above and below the mean taken over the range $|\varepsilon_i|_{i \in 1,2} \le p/2$. The contrast ratio for an embedded feature decays linearly with the square of the PSF diameter as the image resolution degrades; that is, $\rho \propto d^{-2}$.

4.3.2. An array of two alternating features

The intensity profile of an array of alternating features (a,b) is derived by noting that the separation between features a or between features b is equal to twice the pitch, where the pitch is defined as the separation between feature a and its neighbor, feature b. Consequently, the profile is composed of the sum of the profiles of arrays a and b with a pitch of 2γ, where array b is offset from array a by γ along x_1; that is

$$\frac{I}{I_0} = 1 + c_a I_1(\varepsilon_1, l_{1a}, 2\gamma) I_2(\varepsilon_2, l_{2a}) + c_b I_1(\varepsilon_1 + \gamma, l_{1b}, 2\gamma) I_2(\varepsilon_2, l_{2b}) \quad (12)$$

For features of the same size, the above expression is simplified by noting that

$$I_1(\varepsilon_1, l_1, 2\gamma) + I_1(\varepsilon_1 + \gamma, l_1, 2\gamma) = I_1(\varepsilon_1, l_1, \gamma)$$

to reveal contributions similar to those found for the previous sequence:

$$\frac{I}{I_0} = 1 + \{\bar{c} I_1(\varepsilon_1, l_1, \gamma) + \tilde{c}\left[I_1(\varepsilon_1, l_1, 2\gamma) - I_1(\varepsilon_1 + \gamma, l_1, 2\gamma)\right]\} I_2(\varepsilon_2, l_2) \quad (12a)$$

For a dark surface, the above expression is renormalized to $\bar{I}$ to give

$$\frac{I}{\bar{I}} = \left\{I_1(\varepsilon_1, l_1, \gamma) + \frac{\tilde{\eta}}{\bar{\eta}}\left[I_1(\varepsilon_1, l_1, 2\gamma) - I_1(\varepsilon_1 + \gamma, l_1, 2\gamma)\right]\right\} I_2(\varepsilon_2, l_2) \quad (12b)$$

The profiles for $\bar{c} = 0$ and for $\bar{c} \to \infty$ are plotted in Fig. 16.

The expression for the effective contrast is derived from Eq. (12a) for the practical case where the pixel size is matched to the array pitch, which again gives a result that is proportional to the nominal contrast. The ratio of the effective to the nominal

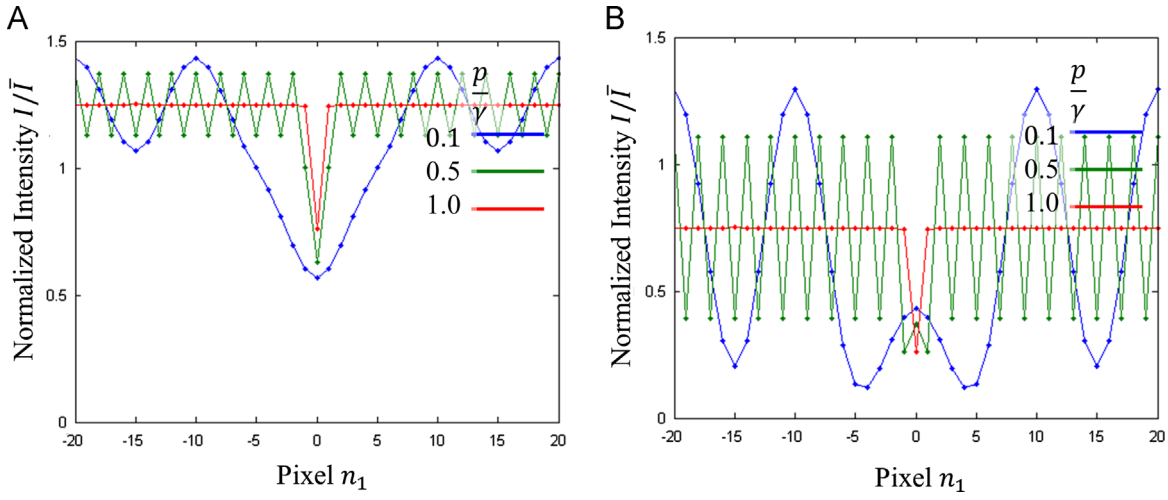

Fig. 14. 1D intensity profile of a new feature embedded in an array of identical features for PSF diameter $d_1 = \gamma$, feature length $l_1 = 0.5\gamma$, feature with $l_2 \to \infty$, offset $\boldsymbol{\varepsilon} = 0$, and reflectivity contrast $\tilde{\eta} = 0.5\bar{\eta}$. (A) The average reflectivity of the two features equals that of the surface, $\bar{\eta} = \eta_0$ ($\bar{I} = I_0$). (B) Dark surface, $\eta_0 = 0$ ($I_0 = 0$).

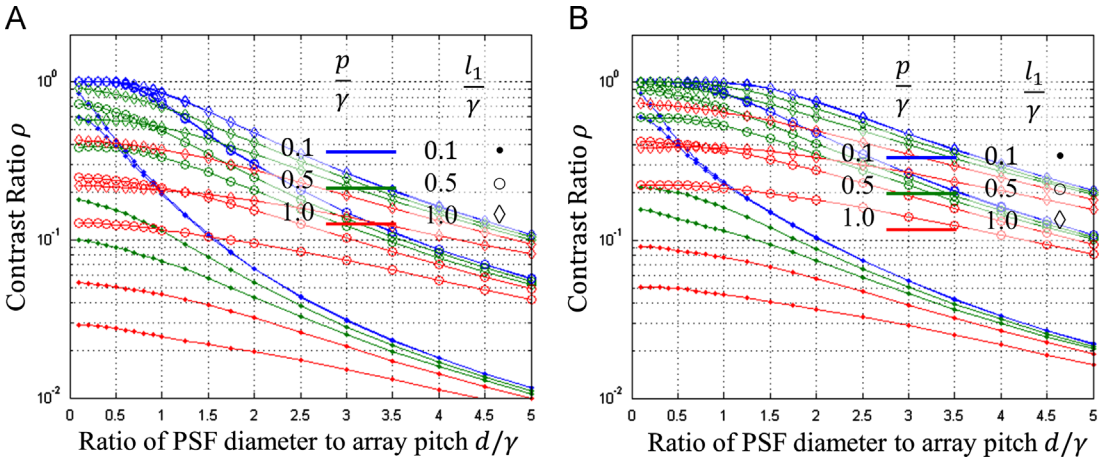

Fig. 15. Ratio of the effective to the nominal contrast of a new feature embedded in an array of identical features for square pixels $p_1 = p_2 \equiv p$, isotropic PSF $d_1 = d_2 \equiv d$, feature lengths $l_{1a} = l_{1b} \equiv l_1$, and feature widths $l_{2a} = l_{2b} = l_2$. There are two curves for each parameter set, which indicate the values that are one standard deviation above and below the mean taken over the offset range $|\varepsilon_i|_{i\in 1,2} \le p/2$. (A) $l_2 = 0.5\gamma$. (B) $l_2 = \gamma$

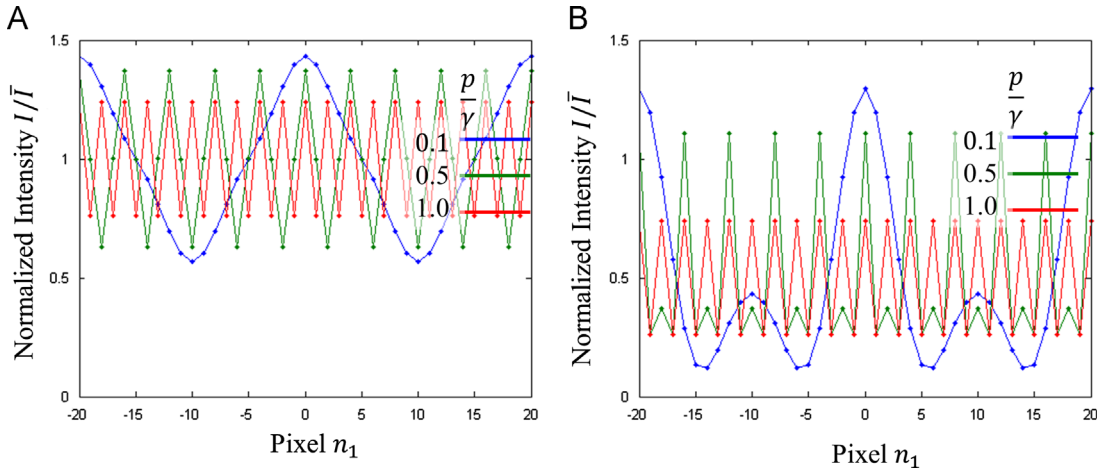

Fig. 16. 1D intensity profile of an array of alternating features for PSF diameter $d_1 = \gamma$, feature length $l_1 = 0.5\gamma$, feature with $l_2 \to \infty$, offset $\varepsilon = 0$, and reflectivity contrast $\tilde{\eta} = 0.5\bar{\eta}$. (A) The average reflectivity of the two features equals that of the surface, $\bar{\eta} = \eta_0 (\bar{I} = I_0)$. (B) Dark surface, $\eta_0 = 0$ $(I_0 = 0)$.

contrast is given by

$$\rho = \frac{1}{2}\Delta\left[I_1(\varepsilon_1, l_1, 2\gamma) - I_1(\varepsilon_1 + \gamma, l_1, 2\gamma)\right] \cdot I_2(\varepsilon_2, l_2) \tag{12c}$$

The contrast ratio is shown in Fig. 17. It represents the loss in the contrast between the two unlike features when imaging with finite optical blur, pixel size, and pixel misalignment. The ratio decays exponentially with the square of the PSF diameter as the image resolution degrades; that is, $\ln \rho \propto -d^2$. This behavior is analogous to that for the intensity contrast of identical features. The dissimilarity is in the coefficient for the exponential decay, which is a factor of four less because of the doubling in the separation of like features.

4.3.3. Sequence images

The sequence of identical features and of the two abovementioned models are spliced and imaged with square pixels and 8 bits of resolution (256 gray levels) in Figs. 18–20. The average reflectivity of the two features in the model sequences is set equal to reflectivity of the surface. Furthermore, the surface gray level is set equal to half the full range or 128 gray levels (GL). The degradation in the feature contrast with an increasing isotropic PSF blur is depicted in the series of sequences from left to right within each image with values of d/γ ranging from 0.1 to 2.5. In addition, Fig. 18 compares the images taken with increasing pixel size, and Fig. 19 shows the effect of the feature-pixel offset. The impact of the nominal contrast is illustrated in Fig. 20.

4.4. Detection of features in the model sequences

The relation between the feature contrast and the detection accuracy is determined by the noise in the pixel gray level. Here, the noise is modeled by a quadrature sum of two contributions: the shot noise, which is associated with the random fluctuation in the number of electrons detected in a pixel over a given period of time; and the noise associated with the electronics of the detection chain. The latter will represent the noise floor of the system.

The shot noise has two contributions: the first is from the random number of electrons incident on the sample surface, N, which for a sufficiently large number is represented by a normal distribution with a mean and variance equal to N; the second is from the statistics associated with the binomial process of reflection, where the incident electron is either reflected or absorbed with the probabilities η and $1-\eta$, respectively. The cascade of a Gaussian distribution followed by a binomial distribution produces a Gaussian distribution for the number of electrons reflected from the surface, N_r. The mean and variance of this distribution are

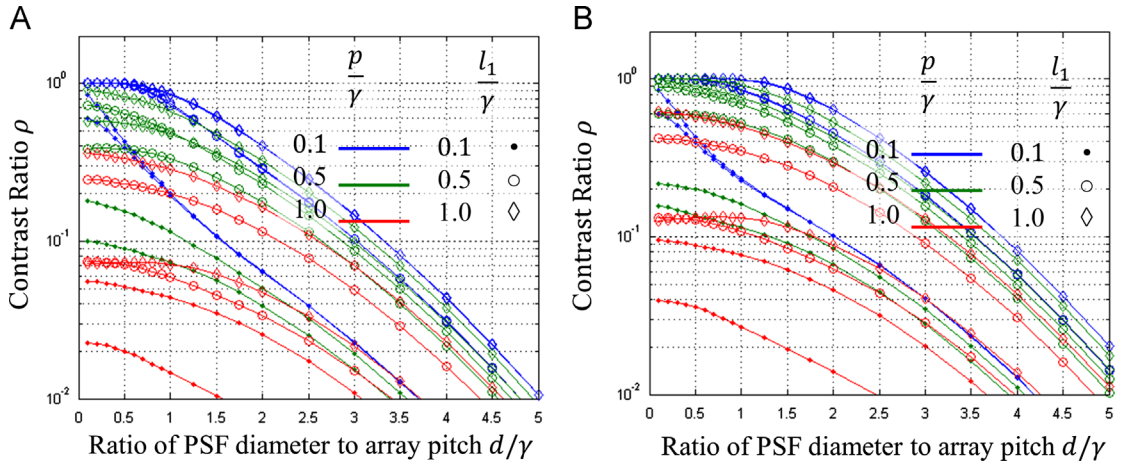

Fig. 17. Ratio of the effective to the nominal contrast in an array of alternating features for square pixels $p_1 = p_2 \equiv p$, isotropic PSF $d_1 = d_2 \equiv d$, feature lengths $l_{1a} = l_{1b} \equiv l_1$, and feature widths $l_{2a} = l_{2b} = l_2$. There are two curves for each parameter set, which indicate the values that are one standard deviation above and below the mean taken over the offset range $|\varepsilon_i|_{i\in 1,2} \le p/2$. (A) $l_2 = 0.5\gamma$. (B) $l_2 = \gamma$.

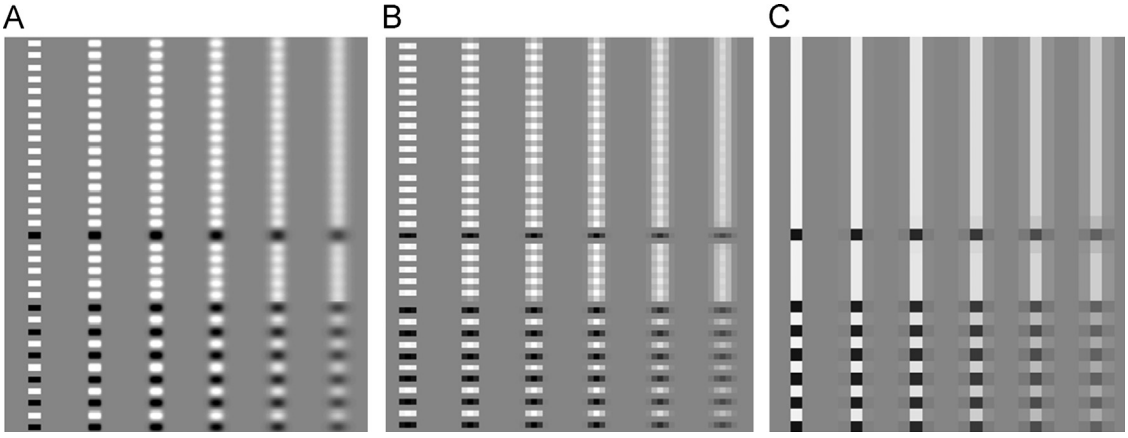

Fig. 18. Images of the three model sequences spliced together illustrating the effect of an increasing pixel size for an isotropic PSF $d_1 = d_2 \equiv d$, nominal feature contrasts $c_a = -c_b = 1.0$, square pixels $p_1 = p_2 \equiv p$, feature lengths $l_{1a} = l_{1b} \equiv 0.5\gamma$, feature widths $l_{2a} = l_{2b} = \gamma$, and offsets $\boldsymbol{\varepsilon_a} = \boldsymbol{\varepsilon_b} = 0$. The spliced sequences are imaged with six PSF diameters increasing from left to right with values of $d/\gamma = (0.01, 0.5, 1.0, 1.5, 2.0, 2.5)$. The gray level limits for presenting [dark, white] are [50, 200]. (A) $p = 0.1\gamma$. (B) $p = 0.5\gamma$. (C) $p = 1.0\gamma$.

found from the law of total expectation and variance to be

$$\langle N_r \rangle = \eta \langle N \rangle$$
$$\langle N_r^2 \rangle - \langle N_r \rangle^2 = \eta(1-\eta)\langle N \rangle + \eta^2 \langle N \rangle = \eta \langle N \rangle$$

The statistics for the number of electrons detected, N_d, is derived from a convolution of N_r with the PSF. Here, it is noted that the distribution for the sum of Gaussian distributed random variables is itself Gaussian with a mean and variance equal to the sum of the mean and variance of the individual distributions. As a result

$$\sigma_{N_d}^2 \equiv \langle N_d^2 \rangle - \langle N_d \rangle^2 = \langle N_d \rangle$$

If the registered current in the pixel, I_d, is proportional to N_d, the distribution for I_d will be represented by the Gaussian function

$$f(I_d) = \frac{dN_d}{dI_d} \frac{1}{\sqrt{2\pi \langle N_d \rangle}} e^{-\frac{1}{2\langle N_d \rangle}(N_d - \langle N_d \rangle)^2} = \frac{1}{\sqrt{2\pi}\sigma_I} e^{-\frac{1}{2\sigma_I^2}(I_d - \langle I_d \rangle)^2}$$

with the standard deviation

$$\sigma_I = \frac{1}{\sqrt{\langle N_d \rangle}} \langle I_d \rangle$$

Adding the standard deviation of the system noise, $\tilde{I}$, in quadrature gives an effective σ_I

$$\sigma_I^* \cong \sqrt{\frac{1}{\langle N_d \rangle} \langle I_d \rangle^2 + \tilde{I}^2}$$

Fig. 21 illustrates the degradation in the image of the model sequences with increasing pixel noise. A feature is defined by having a gray level above or below a given threshold. The probability $F(I_t)$ that the signal in a pixel registers above the threshold I_t is obtained from the cumulative distribution

$$F(I_t) = \int_{I_t}^{\infty} dI_d f(I_d) = \frac{1}{2}\left(1 + \mathrm{erf}\left(\frac{\langle I_d \rangle - I_t}{\sqrt{2}\sigma_I^*}\right)\right)$$

The probability that the signal registers below the threshold is also represented by the above formula provided that the argument of the *Error* function is replaced by its absolute value. For the model sequences, the threshold is set close to the average signal of the two features, $\bar{I}$, making

$$\frac{\left|\langle I_d \rangle - I_t\right|}{\bar{I}} \cong \frac{I_a - I_b}{I_a + I_b}$$

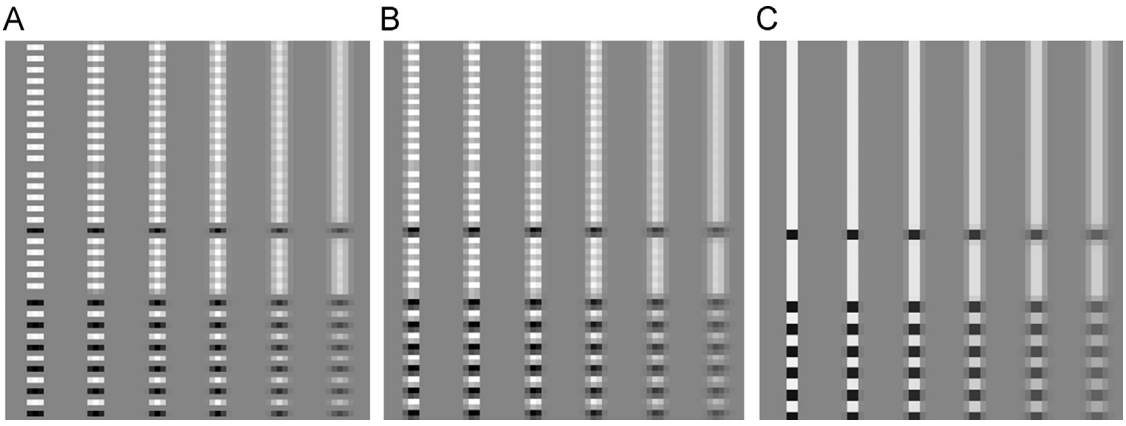

Fig. 19. Images of the three model sequences spliced together illustrating the effect of a non-zero feature-pixel offset for an isotropic PSF $d_1 = d_2 \equiv d$, nominal feature contrasts $c_a = -c_b = 1.0$, pixels $p_1 = p_2 \equiv 0.5\gamma$, feature lengths $l_{1a} = l_{1b} \equiv 0.5\gamma$, and feature widths $l_{2a} = l_{2b} = \gamma$. The spliced sequences are imaged with six PSF diameters increasing from left to right with values of $d/\gamma = (0.01, 0.5, 1.0, 1.5, 2.0, 2.5)$. The gray level limits for presenting [dark, white] are [50, 200]. (A) $\boldsymbol{\varepsilon_a} = \boldsymbol{\varepsilon_b} = 0$. (B) $\boldsymbol{\varepsilon_a} = \boldsymbol{\varepsilon_b} = 0.25(p,p)$. (C) $\boldsymbol{\varepsilon_a} = \boldsymbol{\varepsilon_b} = 0.5(p,p)$.

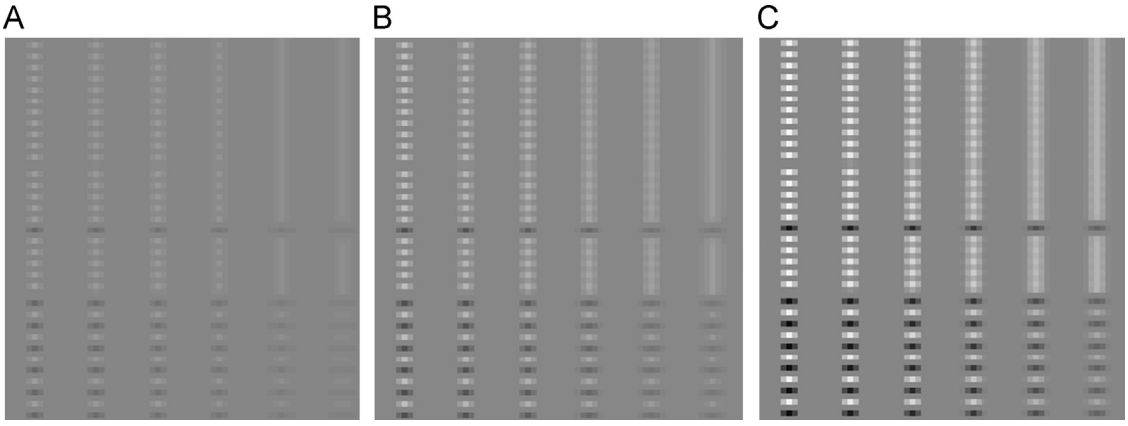

Fig. 20. Images of the three model sequences spliced together illustrating the effect of increasing the nominal contrast for an isotropic PSF $d_1 = d_2 \equiv d$, pixels $p_1 = p_2 \equiv 0.5\gamma$, feature lengths $l_{1a} = l_{1b} \equiv 0.5\gamma$, feature widths $l_{2a} = l_{2b} = \gamma$, and offsets $\boldsymbol{\varepsilon_a} = \boldsymbol{\varepsilon_b} = 0$. The spliced sequences are imaged with six PSF diameters increasing from left to right with values of $d/\gamma = (0.01, 0.5, 1.0, 1.5, 2.0, 2.5)$. The gray level limits for presenting [dark, white] are [50, 200]. (A) $c_a = -c_b = 0.1$. (B) $c_a = -c_b = 0.2$. (C) $c_a = -c_b = 0.5$.

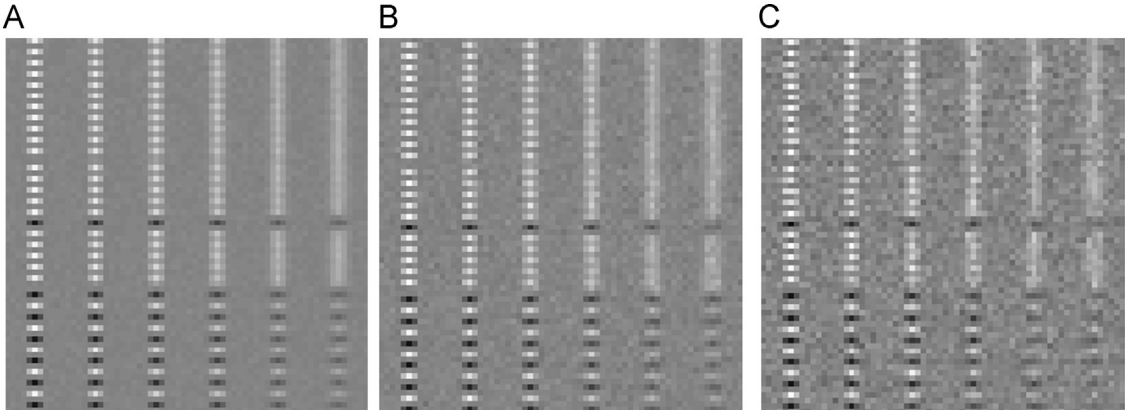

Fig. 21. Images of the three model sequences spliced together illustrating the effect of increasing pixel noise σ_I^* relative to the average signal $\bar{I}$ for an isotropic PSF $d_1 = d_2 \equiv d$, nominal contrasts $c_a = -c_b = 0.5$, pixels $p_1 = p_2 \equiv 0.5\gamma$, feature lengths $l_{1a} = l_{1b} \equiv 0.5\gamma$, feature widths $l_{2a} = l_{2b} = \gamma$, and offsets $\boldsymbol{\varepsilon_a} = \boldsymbol{\varepsilon_b} = 0$. The spliced sequences are imaged with six PSF diameters increasing from left to right with values of $d/\gamma = (0.01, 0.5, 1.0, 1.5, 2.0, 2.5)$. The gray level limits for presenting [dark, white] are [50, 200]. (A) $\sigma_I^*/\bar{I} = 0.01$. (B) $\sigma_I^*/\bar{I} = 0.025$. (C) $\sigma_I^*/\bar{I} = 0.05$.

Approximating $\langle I_d \rangle$ with $\bar{I}$ and $\langle N_d \rangle$ with the corresponding number of electrons, $\overline{N}$, in the expression for σ_I^* gives

$$\frac{I_a - I_b}{I_a + I_b} \cong \sqrt{2\left(\frac{1}{\overline{N}} + \left(\frac{\tilde{I}}{\bar{I}}\right)^2\right)} \cdot \mathrm{erf}^{-1}(2F-1) \tag{13}$$

Fig. 22 illustrates the relation between the feature contrast and the accuracy of detection for a few combinations of $\overline{N}$ and $\tilde{I}/\bar{I}$.

The effective contrast derived from Eq. (13) can be utilized in the plots of Figs. 15 and 17 to determine the nominal contrast required to achieve the desired detection accuracy for the respective model sequences. In particular, for the practical values of $\overline{N} = 2500$ and $\tilde{I}/\bar{I} = 0.025$, Fig. 22 shows that an effective contrast

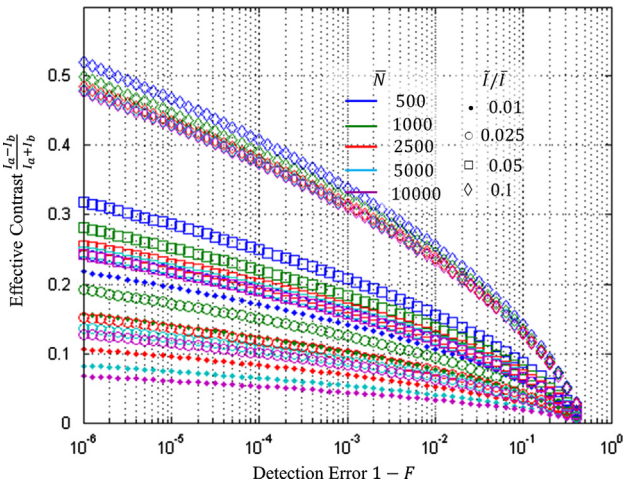

Fig. 22. Required intensity contrast in the features to achieve a given accuracy in their detection for a range of values for the mean number of electrons per pixel $\bar{N}$ and for the standard deviation in the system noise $\tilde{I}$ relative to the mean signal $\bar{I}$.

of 0.15 is required to reduce the error rate to 10^{-6}. If the pixel size is set to 1/2 the pitch (or 0.35 nm for ss-DNA), the PSF diameter is reduced to 2× the pitch (1.4 nm), and the base is assumed to span an area of 0.5 × 1.0 in units of the pitch (0.35 nm × 0.7 nm), then Figs. 15 and 17A give a contrast ratio of ~0.4 for the two model sequences. The nominal reflectivity contrast required between the two bases to give an error rate of 10^{-6} for the aforementioned imaging condition and base geometry is then found to be $\pm 0.15/0.4$ or $\sim \pm 0.4$.

5. Summary and conclusions

The electron-optical concept of MAD-LEEM, a novel microscopy technique utilizing a monochromator, aberration corrector, and dual-beam electron illumination has been presented. Simulations of electron-optical properties of the LEEM objective lens have been completed including aberrations up to 5th order in order to understand the resolution limit with aberration correction. Analysis of electrostatic electron mirrors shows that their negative spherical and chromatic aberration coefficients can be tuned over a large parameter range and used to compensate the aberrations of the LEEM objective lens for a range of electron energies. A novel mirror aberration corrector, an electrostatic pentode mirror, combined with the monochromator has been proposed to further improve the resolution by correcting the 5th order spherical aberration. The tetrode MAC reduces the optical blur to 2.5 nm at 10 eV and 1.5 nm at 100 eV electron energy. The pentode MAC reduces the blur further to 1.2 nm at 10 eV and 0.7 nm at 100 eV electron energy.

A detailed approach for sequencing DNA by imaging in a LEEM has been proposed. Contrast simulations of a model, rectangular nucleotide base geometry with uniform reflectivity show that a nominal reflectivity contrast of less than $\pm 40\%$ between the bases will yield a relatively low error rate of 10^{-6} when sequencing ss-DNA if the microscope resolution is improved to give blur values of ~ 1.5 nm. The requirement on the nominal contrast may be relaxed (or equivalently, the error rate may be lowered) with sub-nm resolution, which according to simulations of the MAD-LEEM electron optics can be achieved by incorporating a pentode MAC and a monochromator. This approach thus has promise to significantly improve the performance of a LEEM for a wide range of applications in the biosciences, material sciences, and nanotechnology where nanometer scale resolution and analytical capabilities are required.

Acknowledgments

The authors would like to thank A.T. N'Diaye and A.K. Schmid at the NCEM, Lawrence Berkeley National Laboratory in Berkeley, CA, and H.H. Persson and Prof. Ron Davis at the Stanford Genome Technology Center in Palo Alto, CA for their support, encouragement and invaluable advice. This project was supported by Grant number R43HG006303 from the National Human Genome Research Institute (NHGRI). The content is solely the responsibility of the authors and does not necessarily represent the official views of the NHGRI or the National Institutes of Health. The authors would also like to thank T.H.P. Chang for his continuous support and numerous suggestions leading to this paper.

References

[1] W. Telieps, E. Bauer, Ultramicroscopy 17 (1985) 57.
[2] H. Hibino, H. Kageshima, F. Maeda, M. Nagase, Y. Kobayashi, H. Yamaguchi, e-Journal of Surface Science and Nanotechnolog 6 (2008) 107.
[3] H.H. Rose, Science and Technology of Advanced Materials 9 (2008) 014107.
[4] H.W. Mook, P. Kruit, Ultramicroscopy 81 (2000) 129.
[5] O.L. Krivanek, J.P. Ursin, N.J. Bacon, G.J Corbin, N. Dellby, P. Hrncirik, M.F. Murfitt, C.S. Own, Z.S. Szilagyi, Philosophical Transactions of the Royal Society A 367 (2009) 1.
[6] M. Mankos, U.S. Patent No. 8,870,172, 22 May 2012.
[7] Electron Optica MG6000, Monochromatic Thermal-field Emission Gun. ⟨www.electronoptica.com⟩.
[8] M.S. Altman, Journal of Physics: Condensed Matter 22 (2010) 084017.
[9] O. Scherzer, Zeitschrift für Physik 101 (1936) 593.
[10] M. Haider, H. Rose, S. Uhlemann, B. Kabius, K. Urban, Journal of Electron Microscopy 47 (1998) 395.
[11] O.L. Krivanek, N. Dellby, A.R. Lupini, Ultramicroscopy 78 (1999) 1.
[12] G.F. Rempfer, M.S. Mauck, Optik 92 (1992) 3.
[13] D. Preikszas, H. Rose, Journal of Electron Microscopy 1 (1997) 1.
[14] Th. Schmidt, H. Marchetto, P.L. Le´vesque, U. Groh, F. Maier, D. Preikszas, P. Hartel, R. Spehr, G. Lilienkamp, W. Engel, R. Fink, E. Bauer, H. Rose, E. Umbach, H.-J. Freund, Ultramicroscopy, 110, 1358.
[15] R.M. Tromp, J.B. Hannon, A.W. Ellis, W. Wan, A. Berghaus, O. Schaff, Ultramicroscopy 110 (2010) 852.
[16] E. Munro, J. Rouse, H. Liu, L. Wang, Journal of Vacuum Science and Technology B 26 (2008) 2331.
[17] W. Wan, J. Feng, H.A. Padmore, D.S. Robin, Nuclear Instruments and Methods in Physics Research A519 (2004) 222.
[18] M. Mankos, D. Adler, L. Veneklasen, E. Munro, Surface Science 601 (2007) 4733.
[19] L.H. Veneklasen, D.L. Adler, U.S. Patent No. 6,803,572, October 12, 2004.
[20] M. Mankos, Nuclear Instruments and Methods in Physics Research A: Accelerators, Spectrometers, Detectors and Associated Equipment 645 (2011) 35.
[21] W.R. Glover III, U.S. Patent No. 7,288,379, 30 October 2007.
[22] W. Andregg, M. Andregg, U.S. Patent Application No. 20,100,267,152, 21 October 2010.
[23] M. Germann, T. Latychevskaia, C. Escher, H.-W. Fink, Physical Review Letters 104 (2010) 095501.
[24] S. Kilina, S. Tretiak, D.A. Yarotski, J. Zhu, N. Modine, A. Taylor, A.V. Balatsky, Journal of Physical Chemistry C 111 (2007) 14541.
[25] R.G. Endres, D.L. Cox, R.R.P. Singh, Reviews of Modern Physics 76 (2004) 195.
[26] X. Guo, A.A. Gorodetsky, J. Hone, J.K. Barton, C. Nuckolls, Nature Nanotechnology 3 (2008) 163.
[27] J.D. Watson, F. Crick, Nature 171 (1953) 737.
[28] A. Bensimon, A. Simon, A. Chiffaudel, V. Croquette, F. Heslot, D. Bensimon, Science 265 (1994) 2096.
[29] M. Mankos, K. Shadman, A. N'Diaye, A. Schmid, H. Persson, R. Davis, Journal of Vacuum Science and Technology B 30 (2012).